
Temporal gene regulation enables controlled expression of gas vesicles and preserves bacterial viability

Received: 20 June 2025

Accepted: 3 December 2025

Cite this article as: Li, Z., Ho, C.-Y., Barr, D.E. *et al.* Temporal gene regulation enables controlled expression of gas vesicles and preserves bacterial viability. *Nat Commun* (2025). <https://doi.org/10.1038/s41467-025-67667-8>

Zongru Li, Chia-Yu Ho, Diana E. Barr, Sumin Jeong, Lihua Ma & George J. Lu

We are providing an unedited version of this manuscript to give early access to its findings. Before final publication, the manuscript will undergo further editing. Please note there may be errors present which affect the content, and all legal disclaimers apply.

If this paper is publishing under a Transparent Peer Review model then Peer Review reports will publish with the final article.

Temporal gene regulation enables controlled expression of gas vesicles and preserves bacterial viability

Zongru Li¹, Chia-Yu Ho¹, Diana E. Barr^{1, 2}, Sumin Jeong¹, Lihua Ma³, and George J. Lu^{1,*}

¹ Department of Bioengineering, Rice University, Houston, TX 77005, USA

² Department of Imaging Physics, University of Texas MD Anderson Cancer Center, Houston, TX, 77030, USA

³ Shared Equipment Authority, Rice University, Houston, TX 77005, USA

* Correspondence: george.lu@rice.edu (G.J.L.)

Abstract

Gas vesicles (GVs) are genetically encodable, air-filled protein nanostructures that have rapidly emerged as a versatile platform for biomedical imaging, cell tracking, and therapeutic delivery. However, in non-native hosts such as *Escherichia coli*, heterologous expression is hampered by a complex assembly involving ~10 proteins, provoking proteotoxic stress and impaired growth. Here we report a reproducible drop in cell density and viability 8–16 hours after GV induction. To address these, we develop a dual-inducer transcriptional system that orthogonally controls assembly factors and the shell protein GvpA2 over a range of stoichiometries. Sequential expression by initiating assembly factors before GvpA2 restores growth without compromising GV production. We further show that the interval between inductions tunes both GV yield and cellular stress. Orthogonal decoupling plus a ~2–3 hours head-start for assembly factors prevents proteotoxicity, preserves yields, and restores viability, establishing a generalizable temporal–stoichiometric design for heterologous expression of multimeric protein nanostructures.

Introduction

Synthetic biology is driving advances in biomedical innovation by harnessing engineered microorganisms as programmable platforms for diagnostics and therapeutics. From tumor-targeting probiotics^{1, 2} to CRISPR-enabled biosensors^{3, 4} and optogenetic systems^{5, 6}, the field is rapidly advancing toward *in vivo* applications where intact, metabolically active cells serve as real-time reporters^{7, 8} or delivery vehicles⁹. Central to these advances is the integration of genetic circuits, such as stress-responsive elements¹⁰ and feedback control systems^{11, 12}, that can reduce metabolic burden and optimize gene expression while preserving host cell viability and function¹³. Such cell-viability-optimized, genetically encodable modules hold the key to enabling broader use of engineered cells for real-time diagnostics¹⁴, targeted drug delivery¹⁵, and adaptive responses *in situ*¹⁶.

Among the genetically encodable modules rapidly advancing in recent years, gas vesicles (GVs), often known as acoustic reporter genes (ARGs)^{17, 18}, are protein-based, air-filled nanostructures naturally produced inside aquatic microorganisms, for buoyancy regulation in their native environments^{19, 20}. Their distinct physical properties, including the inside low density of air^{20, 21}, and a large acoustic impedance mismatch^{18, 22}, have made GVs attractive for many biomedical applications. They have been extensively repurposed as genetically encoded reporters for ultrasound, magnetic resonance imaging (MRI), and optical imaging^{17, 18, 22, 23}. They have also been engineered for deep-tissue acoustic cellular control^{24–26}, pressure sensing²⁷, and targeted delivery to lymph nodes²⁸ and solid tumors^{29, 30}. Additionally, GVs have been engineered into acoustic biosensors capable of detecting enzymatic activities and measuring calcium level

within live cells^{31, 32} to provide insights into dynamic cellular processes. Many of these emerging technologies require GVs to be expressed and function within intact, viable cells to enable real-time, non-invasive monitoring or modulation of cellular behavior *in vivo*. As such, optimizing GV expression for live-cell contexts has become a central focus in advancing its biomedical utility.

However, producing large quantities of GVs in non-native host cells while maintaining optimal cellular physiology remains challenging due to difficulties in assembling the major shell protein, GvpA, into mature GV nanostructures. GvpA is the primary structural component of these GV nanostructures^{19, 20, 33, 34}, conferring a 2–3 nm thick rigid protein shell with a highly hydrophobic inner surface that prevents water condensation^{33, 34}. This shell architecture renders GvpA an amphipathic protein with poor solubility in aqueous environments. Expressing such amphipathic proteins in non-native hosts often leads to misfolding and aggregation, ultimately impairing cell growth and, in some cases, causing lysis. Accordingly, GV operons are consistently observed to encode approximately ten additional proteins, collectively known as assembly factor proteins, which mitigate cellular stress and facilitate the proper assembly of GvpA into mature GV nanostructures through a complex, multi-stage process³⁵. We hypothesize that when expressing GVs in non-native hosts, the stoichiometric ratios and timing of expression between the shell protein and these assembly factors are suboptimal, as the transcriptional regulation mechanisms present in native hosts may be compromised or lose functionality upon transfer to a new cellular context. This may explain why heterologous expression in *E. coli*, even under the strong T7 promoter and IPTG induction, typically yields multiple-fold lower GV production compared to native GV-producing cyanobacteria¹⁷. To address these challenges associated with heterologous GV expression in *E. coli*, we hypothesize that genetic circuit designs from synthetic biology can be used to mitigate cytotoxic effects and improve overall cellular viability.

In this study, we report a drop in *E. coli* cell density occurring 8–16 hours after GV induction. We support this data by transmission electron microscopy (TEM) providing evidence of cell lysis. Colony-forming unit (CFU) assays and flow cytometry analyses reveal a marked decline in cell viability further supporting our data. Next, to address this proteotoxicity, we develop a dual-inducer transcriptional regulation system that enables independent and orthogonal control of GV assembly factors and the shell protein GvpA2 in *E. coli*, allowing precise temporal regulation of gene expression with minimal basal expression or crosstalk. We validate the regulatory properties of the system using fluorescent reporter assays, which demonstrate tight control with low basal expression and effective orthogonality between the two inducible promoters. Leveraging this system, we establish a sequential induction strategy, in which assembly factors expression before GvpA2 restore normal bacterial growth with GV production comparable to its wild-type counterpart. Furthermore, temporal induction analysis reveals that the interval between assembly factors and shell protein expression influences GV yields and cellular stress levels. Decoupling the expression of shell protein and assembly factors and enforcing an assembly factors-first strategy converts GV expression from a construct-tuning approach to an operating principle that preserves viability without reducing yield. Meanwhile, sustained viability enables *in vivo* use and establishes a modular, tunable control strategy portable across complex protein assemblies for biomedical engineering and synthetic biology.

Results

E. coli growth inhibition during GV expression

In this work, we focused on GVs encoded by the pNL29 operon, originally cloned from a truncated portion of the GV operon in *Priestia megaterium* (formerly known as *Bacillus megaterium*)³⁶. The plasmid pST39-

pNL29 (**Fig. 1a**), which carries this operon, has been shown to enable efficient heterologous expression of GVs in *E. coli*^{36, 37}, and has served as the workhorse for constructing acoustic reporter genes (ARGs) and determining cryo-EM structures of GVs^{17, 33}. The pST39-pNL29 plasmid comprises a series of genes for GV assembly, including *gvpA2*, which encodes the primary shell protein GvpA2, followed by genes (*gvpR, N, F, G, L, S, K, J, T, U*) encoding assembly factor proteins. These genes were usually organized under the control of a T7 promoter (T7) and terminator (T7term) to enable robust GV expression in *E. coli*, which can be characterized by transmission electron microscopy (TEM) as hollow and cylindrical nanostructures after purification (**Fig. 1b**). In such systems, GV expression is induced by adding isopropyl β-D-1-thiogalactopyranoside (IPTG), activating the lacUV5 promoter that controls the chromosomally integrated T7 RNA polymerase gene (**Fig. 1c**). T7 RNA polymerase subsequently initiates transcription of the pNL29 operon through its upstream T7 promoter, resulting in the expression of GV proteins (**Fig. 1c**). Notably, the pST39-pNL29 plasmid lacks the lacI repressor and lac operator sequences, allowing for effective induction of GV expression with relatively low IPTG concentrations of 20 μM, which has been used in multiple studies as the optimized induction condition^{28, 35, 37, 38}.

However, we observed signs of compromised cellular growth in overnight cultures across multiple experimental batches. Specifically, following IPTG induction, *E. coli* cultures entered a normal logarithmic phase (log phase), but plateaued around 4 hours post-induction, followed by a marked decline in optical density at 600 nm (OD₆₀₀) commencing around 8 hours post-induction (**Fig. 1d**). This growth arrest and subsequent decline were absent in cultures without IPTG induction (**Supplementary Fig. 1a**). Moreover, increasing the IPTG concentrations to 200 and 400 μM accelerated the onset of growth arrest to approximately an hour post-induction and compounded the decline in OD₆₀₀ to around 2.5 hours post-induction (**Supplementary Fig. 1b, c**). In contrast, control cultures expressing the Maltose-Binding Protein (MBP) and fluorescent protein mCherry displayed a growth trajectory consistent with typical *E. coli* growth patterns (**Fig. 1d** and **Supplementary Fig. 1a, b, and c**), indicating that the growth arrest in GV-expressing cultures is specific to GV expression.

Next, to confirm the hypothesis that substantial cellular toxicity exists around the 8-hour post-induction time window, we conducted TEM characterization on GV-expressing *E. coli* cells. At 4 hours post-induction, TEM images revealed the presence of well-formed, spindle-shaped GVs within intact bacterial cells, indicating successful heterologous expression and assembly of GVs without any cytotoxic effects (**Fig. 1e** and **Supplementary Fig. 2a**). However, by 8 hours post-induction, TEM images demonstrated significant morphological alterations, including compromised cell envelope integrity and leakage of intracellular contents, as evidenced by the presence of GVs outside of cells (**Fig. 1e** and **Supplementary Fig. 2b**). The morphological changes observed by TEM were further evaluated by quantifying cell viability with CFU assays. Following induction with 20 μM IPTG, GV-expressing *E. coli* exhibited a pronounced decrease in colony numbers relative to the growth of MBP controls (**Fig. 1f** and **Supplementary Fig. 3a, c**). This trend was confirmed quantitatively with CFU measurements that show a sharp decline in viability beginning 4 hours after induction and continuing through the 24-hour time course (**Fig. 1g** and **Supplementary Fig. 3b, d**). To complement the CFU assays, we used SYTO 9/PI staining and flow cytometry to analyze viability in individual cells³⁹. Representative scatter plots (**Fig. 1h** and **Supplementary Fig. e**) revealed a higher proportion of PI-positive, membrane-compromised cells in GV-expressing populations compared with MBP controls, particularly evident by 8–12 hours post-induction. Quantification of live and dead populations showed cell viability fell sharply to approximately 20% by 24 hours (**Fig. 1i**), further confirming the severe cytotoxicity induced by GV expression.

Together, these findings demonstrate that while pNL29 GVs can be robustly expressed in *E. coli*, their expression imposes a substantial physiological burden. This proteotoxic stress compromises cellular integrity and leads to growth arrest, loss of viability, and eventual lysis, suggesting a reproducible viability-collapse window (8–16 hours post-induction) that standard single-promoter induction fails to avoid.

Aggregation of GvpA2 cause cellular proteotoxic stress

To investigate the underlying cause of proteotoxic stress observed during the expression of pNL29 GVs in *E. coli*, we focused on GvpA2, the shell protein encoded by the pNL29 operon. GvpA2 is characterized by pronounced hydrophobicity, a feature conserved among GV shell proteins^{20, 40}. A recent cryo-EM study³³ has now further elaborated that GvpA2 monomers possess an exceptionally hydrophobic interior surface that repels water (**Fig. 2a, b**). However, this hydrophobic character also underlies the tendency of GvpA2 and its homologs to aggregate and misfold when overexpressed in heterologous hosts, leading to proteotoxic stress⁴¹. Indeed, when expressing GvpA2 without assembly factors in *E. coli*, we observed an even earlier and more significant decline in OD₆₀₀ (**Fig. 2c**) compared to cultures co-expressing GvpA2 with its assembly factors (**Fig. 1d**). CFU assays and SYTO 9/PI flow cytometry showed a concordant viability trajectory in GvpA2-expressing *E. coli*. Both readouts revealed a sharp decline by 4 hours post-induction, followed by a gradual recovery that approached baseline by 24 hours (**Fig. 2d, e** and **Supplementary Fig. 4**). This rebound in viability can be explained by processes that mitigate proteotoxic stress—sequestration of misfolded proteins into inclusion bodies⁴², which limits interference with essential cellular functions, and population-level adaptation⁴³, including plasmid loss or reduced plasmid copy number, which lowers the burden of toxic protein expression.

In vitro translation of plasmid-encoded GvpA2, unlike control reactions lacking expressed or soluble DHFR, produced visible insoluble aggregates (**Supplementary Fig. 2c**), indicating a cell-independent, intrinsically hydrophobic self-association and precipitation propensity. We further set out to examine whether we can visualize the aggregates of GvpA2 in living cells⁴¹. To this end, we expressed GvpA2 alone, without assembly factors, fused the mCherry fluorescent protein to its the N- or C-terminus and tracked fluorescence signals through microscopy 4 hours post-induction using either 20 μM IPTG (the standard condition used for WT pNL29 GV³⁸) or 400 μM IPTG (a high-expression condition¹⁷ to accelerate T7-driven GvpA2 accumulation and test dose dependence). Unlike the homogeneous fluorescence observed in control cells expressing mCherry alone, both mCherry::GvpA2 and GvpA2::mCherry fusions exhibited distinct fluorescent puncta (**Fig. 2f**), indicative of aggregate formation. To map the sequence elements driving this behavior, we fused mCherry to defined GvpA2 segments. Among all, the constructs containing the second β-strand (β2) produced the most prominent puncta (**Fig. 2g**), consistent with its hydrophobic character³³ (**Fig. 2a**). These findings suggest that the hydrophobic β2 strand dominantly drives GvpA2 aggregation—the major source of proteotoxic stress—making its mitigation essential to optimize GV expression and preserve host physiology.

Engineering a dual-inducer system for orthogonal control of gene expression

To develop an effective strategy for alleviating this expression-associated burden, we drew inspiration from the native regulatory mechanisms that control GV expression in halophilic archaea^{19, 40}. In halophilic archaea such as *Halobacterium salinarum* (*Hbt. salinarum*), GV formation is intricately regulated by the interplay between two transcriptional regulators (**Fig. 3a**): GvpE, an activator, and GvpD, a repressor. These two proteins modulate the expression of gvp gene clusters in two transcriptional directions (**Fig. 3a**). GvpE

binds to upstream activation sequences adjacent to *gvp* promoters, thereby enhancing transcription⁴⁴. Conversely, GvpD represses GV formation by interacting with GvpE, leading to GvpE degradation and subsequent downregulation of *gvp* gene expression⁴⁴. This GvpD and GvpE interaction also has a temporal switch: GvpD is abundant during early growth to prevent premature expression, while its decline in the late exponential phase allows GvpE accumulation and activation of *gvp* gene transcription for GV formation^{45, 46}. This temporal regulatory mechanism ensures tightly controlled GV production and allows cells to respond to environmental conditions and maintain cellular homeostasis.

Inspired by this native regulatory mechanism, we developed a dual-inducer transcriptional regulation system (mentioned as ‘dual-inducer system’ in later texts; **Fig. 3b**) to mitigate the proteotoxic stress. In an example design, assembly factor genes can be placed under the control of a T7 promoter, with transcription initiated by T7 RNA polymerase upon induction with IPTG. Meanwhile, shell protein gene expression in the inverted transcriptional direction is regulated by a tetracycline-responsive promoter (anhydrotetracycline (aTc)-inducible system⁴⁷), wherein transcription is repressed by the Tet repressor (TetR) and derepressed upon aTc addition. This modular system provides orthogonal induction inputs that allow for independent GV component expression dynamics (**Fig. 3b**). Specific assembly factors have been identified as potential chaperones that interact with the hydrophobic shell protein GvpA2, preventing its premature aggregation and facilitating proper assembly into the GV structure^{35, 40}. Therefore, by decoupling the expression of shell protein and assembly factors, this system aims to enable independent and temporal control over each of them, thereby minimizing the cellular proteotoxic stress from misfolded GvpA2 aggregates and improving growth inhibition during GV expression.

Validating low basal activity and orthogonal control of the dual-inducer system by fluorescent reporters

First, we aim to establish the induction strength and orthogonality of the engineered dual-inducer system. To this end, we utilized fluorescent reporters, sfGFP and mCherry, as proxies for shell protein and assembly factors, respectively (**Fig. 4a**). Induction-specific fluorescence fold-changes were quantified for each module and compared against single-reporter controls (**Fig. 4b**). IPTG-induced mCherry expression in the dual-inducer construct exhibited lower fold-change values across all tested IPTG concentrations relative to the single-reporter control (**Fig. 4c**). This reduction likely reflects the metabolic burden^{12, 48} from constitutive TetR expression, decreasing available cellular resources. Conversely, the aTc-induced sfGFP expression in the dual-inducer system showed fold-change values comparable to the single-reporter control across all tested aTc concentrations (**Fig. 4d**), underscoring the robust independence of the aTc-inducible system regulatory module within the dual-inducer system. Next, to evaluate basal expression levels of each inducible module, we measured fluorescence intensity fold-change without induction in the dual-inducer system relative to single-reporter controls. Basal mCherry expression (0 μM IPTG; varying aTc) in the dual-inducer construct showed reduced fold-change compared to the mCherry-only control (0 μM IPTG; **Fig. 4e** and **Supplementary Fig. 6a**). Similarly, basal sfGFP expression (0 ng/mL aTc; varying IPTG) closely matched the minimal baseline from the sfGFP-only control (**Fig. 4f** and **Supplementary Fig. 6b**). These observations indicate minimal leakage and stringent repression of both IPTG- and aTc-inducible modules under uninduced conditions.

We next assessed potential regulatory interference within the dual-inducer system under simultaneous induction conditions. At constant aTc induction (500 ng/mL), fold-change in mCherry fluorescence remained comparable between cultures with and without aTc at lower IPTG levels (0 and 20 μM, **Fig. 4g, h**). However, higher IPTG concentrations (200 and 400 μM) exhibited reduced mCherry fluorescence upon

aTc co-induction (**Fig. 4h**), indicative of resource competition. A similar trend in inducibility and resource competition was observed for sfGFP (**Fig. 4i**); because the fold decrease at 200 and 400 μ M was comparable, we fixed IPTG at 200 μ M for the aTc titration in the other half of the dual-inducer system (**Fig. 4j–l**) to demonstrate interference while avoiding the additional global load and dynamic-range compression at 400 μ M. To further preclude potential biases arising from the differing fluorescence properties of sfGFP and mCherry, we interchanged their regulatory controls within the dual-inducer system (**Supplementary Fig. 6a**). Results were consistent with previous observations on functionality, basal expression levels, and unintended regulatory interference (**Supplementary Fig. 6** and **7**). Collectively, these findings validate that the dual-inducer system maintains precise regulatory control, minimal basal expression, and minimal unintended interference, as demonstrated by its consistent performance irrespective of the specific fluorescent reporters employed.

Expressing assembly factors before the shell protein alleviates proteotoxic stress and restores *E. coli* growth

Next, we aimed to assess whether implementing this system to achieve sequential expression of assembly factors before shell protein synthesis could alleviate proteotoxic stress and restore *E. coli* growth during GV expression. Based on the rapid protein accumulation typically observed within 2–4 hours in T7-driven systems⁴⁹, we selected a 3-hour interval between each induction to ensure sufficient expression of assembly factors to effectively chaperone GvpA2³⁵. To further investigate how varying the expression levels of assembly factor proteins and shell protein influence *E. coli* growth, we initially induced cultures with a range of IPTG concentrations, followed by a constant aTc concentration of 500 ng/mL after 3 hours (**Fig. 5a**). In another set of screening, cultures were first induced with a fixed IPTG concentration of 200 μ M, and subsequently exposed to varying aTc concentrations after the same 3-hour interval (**Fig. 5b**). For the IPTG-regulated assembly factors induction screening, all groups except the uninduced one (0 μ M IPTG) exhibited restored *E. coli* growth patterns, characterized by the absence of the growth arrest or OD₆₀₀ decline observed in cells expressing the wild-type pNL29 GV operon (**Fig. 5c**). In contrast, the 0 μ M IPTG exhibited a marked decline in OD₆₀₀ from approximately 5 hours after aTc-regulated induction of the shell protein to the second day. Notably, this decline occurred later than in cells expressing GvpA2 alone under the T7-driven system (**Fig. 2c**). One plausible explanation to this observation is that the aTc-inducible system, which utilizes endogenous *E. coli* RNA polymerase⁵⁰, exhibits comparatively lower expression levels than the T7-driven system, as T7 RNA polymerase transcribes roughly 5–8 times faster than *E. coli* RNA polymerase^{49, 51}. For the aTc-regulated assembly factors induction screening, all experimental groups exhibited restored *E. coli* growth profiles, with only a minimal decrease in OD₆₀₀ observed approximately 2 hours after aTc-induced shell protein expression (**Fig. 5d**). Consistent with these growth measurements, CFU assays (**Fig. 5e, f**; **Supplementary Fig. 8a, b**; **Supplementary Fig. 9a, b**) and SYTO9/PI flow cytometry (**Fig. 5g**; **Supplementary Fig. 8c, d**; **Supplementary Fig. 9c, d**) further confirmed that sequential induction markedly improved cell viability across a range of inducer concentrations. In contrast, cultures lacking assembly factor induction (0 μ M IPTG) exhibited noticeable reductions in both CFU and flow cytometry viability, consistent with the observed growth defects in OD₆₀₀ tracking. These results further demonstrate that early expression of assembly factors buffers cells against the proteotoxic effects of premature shell protein accumulation. Meanwhile, the OD₆₀₀ values for both screenings at the 24-hour post-induction harvest point were consistently lower than those observed in the MBP control group (**Fig. 1d**), reflecting the metabolic cost of producing complex nanostructures in *E. coli*⁵² and potentially limiting maximal cell density. However, CFU and flow cytometry analyses showed that cell viability in all dual-

inducer groups was comparable to MBP controls, indicating that while maximal cell density remains limited, the sequential induction strategy effectively alleviates both proteotoxic stress and the metabolic burden associated with GV expression.

Interchanged regulatory control limits the mitigation of proteotoxic stress in *E. coli*

Building upon the demonstrated interchangeability of the dual-inducer system using fluorescent proteins, we sought to evaluate whether swapping the regulatory controls of assembly factors and GvpA2 would yield comparable mitigation of proteotoxic stress. In the early ARG development¹⁷, the entire GV operon was placed under IPTG control, which led us to hypothesize that maintaining IPTG control for GvpA2 would similarly optimize GV yield. Thus, we designed a configuration in which GvpA2 expression was induced by IPTG, while assembly factors expression was controlled by aTc (**Fig. 6a**). However, the outcome was somewhat unexpected. OD₆₀₀ profiles were assessed using the same methodology as previously described (**Fig. 6b, d**). Although the growth arrest characteristic of the wild-type was not observed, all groups, except the uninduced GvpA2 group (0 μM IPTG), displayed a noticeable decrease in OD₆₀₀ commencing approximately 3–9 hours post IPTG-regulated shell protein induction (**Fig. 6c, e**). Similarly, CFU trajectories showed an early but gentle deficit (4–8 hours) after IPTG-induced GvpA2 expression but rebounded to ~10¹⁰–10¹¹ CFU/mL by 24 hours when assembly factors were present (**Fig. 6f** and **Supplementary Fig. 10a, b**). In the reciprocal screening (IPTG fixed at 200 μM), withholding assembly factors (0 ng/mL aTc) produced the deepest and most persistent CFU loss, whereas 50–1000 ng/mL aTc restored CFU to near MBP levels by 24 hours (**Fig. 6g** and **Supplementary Fig. 11a, b**). Flow-cytometry viability mirrored these trends: viability dipped at 8 hours and returned to ~70–76% by 24 hours with assembly-factor expression, remained relatively low without aTc (**Fig. 6h; Supplementary Fig. 10c, d; Supplementary Fig. 11c, d**). This observation may also be attributed to the inherently lower transcriptional strength of the aTc-inducible system⁵⁰ compared to the T7-driven system^{49, 51}. The interchanged regulatory configuration provides only partial mitigation—adequate aTc restores CFU and viability by 24 hours, yet early proteotoxic stress persists and overall performance remains inferior to MBP controls—underscoring the advantage of front-loading assembly-factor expression. Therefore, the stoichiometric balance between assembly factors and the shell protein determines outcomes: when GvpA2 production outpaces chaperoning capacity—e.g., T7-driven GvpA2 paired with aTc-limited assembly factors—cultures show early OD₆₀₀ decline and CFU/viability deficits.

The dual-inducer system achieves GV yields comparable to the wild-type operon in *E. coli*

Having established that the dual-inducer system alleviates proteotoxic stress and restores growth, we next tested whether the sequential expression of assembly factors and GvpA2 affects GV yield in *E. coli*. In this yield analysis, “wild-type control” denotes the heterologous expression of the pNL29 operon (from *P. megaterium*) in *E. coli*. This system serves as the field’s benchmark^{17, 33, 52, 53} since GV production has not been established in the native organism^{36, 37}. The hydrostatic collapse assay is a quantitative method used to assess GV yield by measuring the susceptibility of GVs to pressure-induced collapse^{38, 54}. In this technique, a suspension of purified GVs is subjected to incrementally increasing hydrostatic pressure, and the corresponding decrease in optical density at 500 nm (OD₅₀₀) is monitored (**Fig. 7a**). The reduction in OD₅₀₀ reflects the collapse of GVs, as intact GVs scatter light²⁰, resulting in a turbid appearance, whereas collapsed ones lose this scattering property, yielding a clear solution (**Fig. 7b**). The pressure-dependent changes in OD₅₀₀ of GV samples can be normalized and fitted using a Boltzmann sigmoidal regression model³⁷, with the goodness-of-fit assessed through the coefficient of determination (*R*²) (**Fig. 7c**). In

low-yield or assembly-impaired conditions, the GV-specific dynamic range of OD₅₀₀ is small and variable across replicates, which inflates the normalized variance at high pressure. We lysed cells expressing GVs at harvest and subsequently employed the hydrostatic collapse assay to quantitatively determine GV yield in each culture, as GVs are the primary cellular component responsible for OD₅₀₀ reduction. The hydrostatic collapse profile of cultures expressing the wild-type pNL29 GV operon induced with 20 μM IPTG served as the control, due to this group's highest coefficient of determination (**Fig. 7d-f**), indicative of substantial GV production. Interestingly, at 0 μM IPTG induction, the *R*² value (**Fig. 7d**) was higher than that observed at 200 μM IPTG (**Fig. 7e**) and 400 μM IPTG (**Fig. 7f**). At 0 μM IPTG, basal leak produced limited GVs (moderate *R*²), whereas ≥ 200 μM IPTG yielded poor logistic fits and near-linear OD-pressure profiles, consistent with a weak GV signal superimposed on pressure-insensitive background turbidity arising under proteotoxic stress. Together, these data support an optimum at 20 μM IPTG: lower and higher regimes fall outside the assembly window and deviate from the expected sigmoidal collapse.

Next, to ask whether the sequential expression impacts GV production yield in *E. coli*, we utilized the abovementioned screening protocol (**Fig. 5a, b**). In the IPTG-regulated assembly factors induction screening, all induced groups exhibited hydrostatic collapse profiles comparable to the value of the wild-type pNL29 GV operon induced at 20 μM IPTG, as demonstrated by comparable *R*² values to the wild-type counterpart (**Fig. 8a**). Notably, the *R*² value at 20 μM IPTG is not as high as those at higher IPTG concentrations. This observation indicates a lower GV yield at 20 μM IPTG, consistent with the previously recorded OD₆₀₀ profiles (**Fig. 5c**), which reflects a reduced metabolic burden due to lower GV expression. To further substantiate these results, we calculated the reduction in OD₅₀₀ and normalized it to OD₆₀₀ at harvest to account for variations in cell density. As higher normalized reduction values correlated with increased GV yield, the results (**Fig. 8b**) demonstrated consistent trends with the hydrostatic collapse profiles. All IPTG-induced groups exhibited normalized reduction values comparable to the wild-type, demonstrating the efficacy of the dual-inducer system in maintaining GV production. In the aTc-regulated shell protein induction screening, groups induced at higher aTc concentrations exhibited hydrostatic collapse profiles comparable to that of the wild-type control (**Fig. 8c**). In contrast, the low *R*² value observed at 50 ng/mL aTc indicates a marginal GV yield, corroborated by the lower normalized OD₅₀₀ reduction compared to groups induced with higher aTc concentrations (**Fig. 8d**). Reduced yield likely reflects limited GvpA2 expression from the aTc-inducible module at low aTc, leaving insufficient shell protein for efficient GV assembly.

GVs were also purified from all groups simultaneously using the centrifugation-assisted flotation³⁸ (**Fig. 8e**). We measured the OD₅₀₀ for each sample and normalized to the OD₆₀₀ of the corresponding cultures at harvest. High normalized OD₅₀₀ values indicate greater GVs, as intact GVs effectively scatter light, resulting in increased turbidity²⁰. In both the IPTG- and aTc-regulated induction screenings, GVs were successfully purified, except for the non-induced and the 50 ng/mL aTc groups, from which no GVs were recovered in purification. All experimental groups exhibited normalized OD₅₀₀ values comparable to the wild-type control value, although the 1000 ng/mL aTc group displayed marginally reduced normalized OD₅₀₀ values, indicating slightly lower GV production (**Fig. 8f**).

GV yield under the interchanged regulatory configuration (**Fig. 6a, b, d**) was also assessed by hydrostatic collapse assays on lysed cell cultures. Consistently low *R*² values (**Fig. 8g, h**) indicate no group demonstrated substantial GV production. This outcome is conceivably due to the limited expression of assembly factor proteins under the aTc-inducible system, whose transcriptional strength is insufficient⁵⁰ to express the amount of assembly factors for effective GV assembly. In conclusion, our results demonstrate

that the sequential expression of assembly factors prior to shell proteins maintains GV yields comparable to those of the wild-type pNL29 operon, while preserving bacterial viability.

Time windows of the sequential induction influence cellular stress mitigation and GV yield

Lastly, to investigate the impact of induction timing on the performance of the dual-inducer, we examined whether varying the interval between the initiation of assembly factor protein expression and shell protein expression influences system efficacy. Given that the molar ratio between assembly factors and shell protein is critical for maintaining cellular fitness and proper GV assembly^{18, 35, 55}, we screened time intervals between inductions (**Fig. 9a**) to evaluate the influence on restoring cell viability and the efficiency of GV formation.

In groups shell protein was induced before assembly factors (**aTc (-2 h) and aTc (-1 h)** in **Fig. 9a**), substantial variability was observed in OD₆₀₀ profiles (**Fig. 9b** and **Supplementary Fig. 12**). CFU trajectories for the -2 h and -1 h groups kept dropping after aTc induction and remained low through 24 hours post-induction (**Fig. 9c** and **Supplementary Fig. 13a, c**). SYTO 9/PI flow cytometry showed a consistent pattern, with a low viability range at ~31–42% 8–12 hours and below 30% at 24 hours post-induction (**Fig. 9d** and **Supplementary Fig. 14**). These data indicate a sustained viability deficit when the shell protein precedes assembly factors, with little evidence of recovery. Among the replicates that grew, GV yields were markedly lower than in wild-type cultures (**Fig. 9e**). These findings suggest that premature expression of GvpA2 without sufficient assembly factors may cause GvpA2 aggregation due to insufficient chaperoning, leading to proteotoxic stress and reduced cell viability.

Meanwhile, OD₆₀₀ tracking indicated restored bacterial growth profiles in all remaining groups (**Fig. 9f**). Specifically, initiating IPTG at culture start exhibited a log phase growth comparable to the wild-type control but without subsequent growth arrest (**IPTG (start)** in **Fig. 9f**), suggesting minimal cellular stress associated with expressing assembly factors alone. Simultaneous induction of shell and assembly factors produced a brief post-induction lag relative to wild-type yet maintained viability (**aTc (0 h)** in **Fig. 9f**), consistent with the lower transcriptional strength of the aTc-inducible⁵⁰ module versus T7^{49, 51}, which limits GvpA2 relative to assembly factors and enables effective chaperoning. The highest final OD₆₀₀ occurred when assembly factors preceded shell expression by 2 hours (**aTc (2 h)** in **Fig. 9f**). Longer induction intervals supported growth with minimal declines in OD₆₀₀ following induction (**aTc (3, 4, 5, and 6 h)** in **Fig. 9f**). Complementary to these growth profiles, CFU trajectories for all dual-inducer schedules remained high through 24 hours, contrasting with the decline of the wild-type (**Fig. 9g** and **Supplementary Fig. 13b, c**). Flow cytometry heat maps showed that cell viability across groups was comparable to or exceeding the MBP control and far above the wild-type (**Fig. 9h** and **Supplementary Fig. 14**). Furthermore, all groups, except those with induction intervals of 4, 5, and 6 hours, demonstrated GV yields comparable to the wild-type control (**Fig. 9i**). The reduced GV yields observed in these longer-interval groups may reflect that cells had already reached high density, where nutrient limitation⁵⁶ constrains shell-protein expression and final GV assembly.

In sum, our results demonstrate the existence of an optimal induction interval (~2–3 hours) between shell assembly factor protein expression, which allows proper stoichiometric balance, mitigates proteotoxic stress, and supports efficient GV assembly. These insights establish a basis for future optimization of GV production in heterologous hosts and may also inform the development of programmable expression systems for other complex macromolecular assemblies.

Discussion

The protein-based nanostructures, GVs, exhibit distinct physical properties that enable them to be repurposed for a range of biomedical applications. Their genetic encodability further allows their use as programmable components within synthetic biology systems. However, the heterologous expression of GVs in microbial hosts encounters challenges due to proteotoxic stress^{35, 52}. This stress arises from the aggregation-prone nature of the shell protein GvpA2⁴¹, which is detrimental to cellular viability. Maintaining robust cellular viability is crucial for biomedical and biotechnological applications. Healthy host cells not only ensure reproducible and reliable results but also directly impact the effectiveness and safety of therapeutic interventions in clinical contexts⁵⁷. In this way, GV-triggered proteotoxic stress compromises the reliability and efficacy of GV-based technologies. To address proteotoxicity, we developed a dual-inducer transcriptional regulation system engineered to sequentially express assembly factors before inducing GvpA2. This strategy enabled the sufficient accumulation of assembly factors capable of chaperoning GvpA2, facilitating proper folding and GV assembly. As a result, we successfully mitigated proteotoxic effects, restored bacterial growth, and achieved GV yields comparable to those obtained with the wild-type operon. These findings also articulate a potential temporal–stoichiometric design for heterologous expression of multimeric protein assemblies to enhance their host viability.

Our results in interchanged regulatory studies (**Fig. 6** and **Fig. 8g, h**) and temporal induction screenings (**Fig. 9**) indicate that the assembly of GVs relies on precise stoichiometry and temporal relationship among shell and assembly factor proteins in the pNL29 operon. This balance is essential for the successful assembly of GV nanostructures⁴⁰, as an excessively high molar ratio of shell proteins to assembly factors can result in shell protein aggregation, inadequate assembly support, and cytotoxicity, whereas an excessively low ratio may cause inefficient energy utilization due to surplus assembly factors relative to available shell proteins, thus limiting overall GV production. Therefore, achieving this balance requires finely-tuned expression control. As an alternative to T7 and aTc-inducible systems in this study, pBAD has been used to drive a *Serratia*-derived GV cluster in *E. coli* for *in vivo* applications, illustrating that weaker, tightly tunable promoters can support functional GV expression with a reduced burden⁵². This study motivates testing other expression modules for GV proteins to preserve viability while maintaining or improving yield.

Although our experiments center on the *P. megaterium*'s operon in *E. coli*, the mechanism we target—proteotoxicity from disproportionate shell protein expression and its mitigation by prior accumulation of assembly factors—arises from features conserved across GV systems. Shell subunits (GvpA/B family) are small, β-rich, and strongly hydrophobic^{20, 33, 34, 40}, whereas assembly factors (e.g., GvpF/G/J/K/L/M and the AAA⁺ ATPase GvpN) orchestrate nucleation, elongation, and quality control^{19, 35, 40}. In heterologous hosts, failure typically occurs when GvpA-like proteins outpace assembly capacity due to proteostasis and aggregate^{35, 41}. Consistent with this view, only a limited set of operons has produced GVs in *E. coli* (e.g., *P. megaterium*-derived pNL29, *D. Anabaena*-derived ARG clusters, *Serratia* sp. 39006, and a *Desulfobacterium vacuolatum* operon), whereas many others screened under standard conditions do not assemble⁵²; notably, haloarchaeal clusters have not been demonstrated to form GVs in *E. coli*. These outcomes suggest that qualitative design rules are shared, but quantitative optima—promoter/RBS strength⁵⁸, copy number⁵⁹, induction timing⁶⁰, and, in some cases, host context (ionic strength, temperature, chaperone capacity)^{52, 61}—are cluster-specific. The dual-inducer architecture is therefore portable but parametrically tunable: by enforcing an assembly factor-first sequence and independently adjusting dose and timing, it provides a practical template for adapting expression to diverse GV gene sets.

An important next step is to unravel the underlying molecular mechanism behind this optimal stoichiometry, specifically by investigating the protein complexes and interactions that govern the assembly

process. However, studying these relationships is challenging because: (1) the dynamic and transient nature of protein-protein interactions during GV formation^{35, 40} and (2) the difficulty in isolating and quantifying individual proteins within the complex assembly process^{35, 62}. Recent methodological advances, such as split-GFP assays and affinity-based pull-down techniques⁶², have provided promising approaches to capture transient interactions among GV proteins under physiologically relevant, high-salt conditions. A recent study from our lab advanced this effort by deploying a high-throughput interaction screen in living cells to systematically map interactions among all 11 GV proteins encoded in the pNL29 operon³⁵. This work resolved key nodes in the protein-protein interaction network, including chaperone-like partnerships and stoichiometric dependencies between structural regulators. These datasets provide a framework for rational engineering of genetic circuits controlling each GV protein in the future, ensuring empirical optimization of cellular physiology, GV yields, and potentially, their physical properties. Guided by this interaction map, yield could also be increased by tuning expression stoichiometry and timing: promoter/RBS libraries⁶³ and plasmid copy-number variants⁶⁴ to set the ratios between GV proteins; staged induction to modulate nucleation (GvpF/G/J) versus elongation (GvpN/R); and host-level measures that elevate proteostasis capacity, such as GroEL/ES co-expression⁶⁵, reduced temperature⁴³, or controlled growth rate⁶⁶. These circuit- and host-level interventions are orthogonal to protein design and can be layered onto the dual-inducer framework to expand the production window while preserving viability. Engineering GV proteins genetically may also offer a strategy to improve GV assembly. Recent work demonstrated that directed evolution of GvpA in *E. coli* can increase GV production and enhanced acoustic signals⁵³. In parallel, rational design by leveraging the cryo-EM structure of shell proteins^{33, 34} could enable targeted residue modifications to refine solubility, thermostability, or interfacial interactions between assembly components.

Beyond addressing the assembly challenge of GVs, our dual-inducer system may provide a model for optimizing the assembly of other multimeric protein assemblies, ranging from self-assembling protein nanocompartments⁶⁷ to biomolecular condensates⁶⁸ that require finely tuned temporal expression and stoichiometry. For instance, carboxysomes often employ a “core-first” assembly strategy⁶⁷, where sequential incorporation of components is critical for efficient biogenesis. Transferring operons into heterologous hosts may disrupt these established temporal patterns, and synthetic circuits like our dual-inducer system, which enable orthogonal and temporally resolved gene expression, can re-establish native-like sequential logic and promote optimal assembly. Beyond structural systems, this dual-input paradigm is directly applicable to engineered feedback loops and synthetic oscillators. Dual-input regulation has been shown to independently modulate amplitude and period in synthetic gene circuits⁶⁹. Leveraging this capability, our dual-inducer design has the potential to effectively integrate fast and slow feedback motifs⁷⁰ and facilitate robust and noise-resistant switching⁷¹ behaviors analogous to those observed in natural biological contexts. Therefore, our framework also provides a powerful tool for dynamic regulation in broader synthetic biology applications.

In summary, our study presents a dual-inducer transcriptional regulation system that effectively mitigates proteotoxic stress associated with heterologous expression of GVs in *E. coli* by sequentially controlling assembly factors and the shell protein. This sequential induction restored cellular viability while maintaining GV yields equivalent to wild-type operon expression. The detailed investigation into optimal temporal induction intervals underscored the critical role of stoichiometric balance between shell and assembly factor proteins for efficient GV assembly. These findings establish a tractable framework for further refining synthetic genetic circuits, protein engineering, and mapping the molecular interactions that govern GV biogenesis. By resolving kinetic and stoichiometric bottlenecks, this work advances the

potential for tunable and scalable production of GV-based tools for biomedical engineering and synthetic biology.

ARTICLE IN PRESS

Methods

Ethics declarations

All authors meet the authorship criteria as defined by Nature Portfolio journals, having made substantial contributions to the conception, design, execution, or interpretation of the study. Roles and responsibilities were agreed upon prior to the commencement of the research. Contributors who did not meet all criteria for authorship are acknowledged in the Acknowledgements section. This research was conducted in collaboration with local partners to ensure relevance and applicability to the local context. The study design and implementation were carried out with respect for local norms and practices. Efforts were made to prevent any form of stigmatization, discrimination, or personal risk to participants. Relevant local and regional research has been appropriately cited to acknowledge existing contributions and to provide context. Relevant local and regional research has been appropriately cited to acknowledge existing contributions and to provide context.

Plasmids construction

The plasmid pST39-pNL29, encoding the gas vesicle (GV) gene cluster from *Priestia megaterium* (formerly *Bacillus megaterium*), was obtained from Addgene (plasmid #91696). The GV gene cluster sequence corresponds to GenBank accession number AF053765.1. The major shell protein, GvpA2, is derived from *P. megaterium* and is cataloged under UniProt ID O68677 (GVPA2_PRIMG). Structural representations of GvpA2, as depicted in **Fig. 2a, b** by using ChimeraX⁷² (version 1.9), were adapted from cryo-electron microscopy (cryo-EM) data available in the Protein Data Bank (PDB 7R1C)³³. The plasmid pAJM.011, incorporating the Tet repressor (TetR) and the tetracycline-responsive promoter (aTc-inducible system)⁵⁸, was sourced from Addgene (plasmid #108529). The monomeric Cherry red fluorescent protein (mCherry) gene was obtained from Addgene (plasmid #29747), and the superfolder green fluorescent protein (sfGFP) gene was acquired from Addgene (plasmid #85492). Oligonucleotides for molecular cloning were synthesized by Integrated DNA Technologies (IDT, Coralville, IA). All genes of interest were cloned into the pST39 vector backbone using the NEBuilder® HiFi DNA Assembly Master Mix (New England Biolabs, Ipswich, MA) or KLD Enzyme Mix Reaction (New England Biolabs, Ipswich, MA), following the manufacturer's protocol. All primers and plasmids details can be found in the Supplementary Data 1.

Recombinant GV expression in *E. coli*

Chemically competent BL21 Star™ (DE3) pLysS One Shot™ *E. coli* strain (Thermo Fisher Scientific, Waltham, MA) was transformed with 1 µL of 10 ng/µL plasmid DNA—either wild-type pST39-pNL29 and GvpA2 only or dual-inducer transcriptional regulation system variants—using the heat shock method. The plasmid DNA was gently mixed with 10 µL of competent cells and incubated on ice for 30 minutes. Cells were then subjected to a 30-second heat shock at 42 °C, followed by immediate placement on ice for 5 minutes. Subsequently, 400 µL of pre-warmed SOC medium (Thermo Fisher Scientific, Waltham, MA) was added to each transformation reaction, and the cells were incubated at 37 °C for 1 hour with shaking at 250 rpm to allow recovery. Transformed cells were then plated on LB (Luria-Bertani) Miller agar plates (Thermo Fisher Scientific, Waltham, MA) with 1% glucose, 25 µg/mL chloramphenicol (MilliporeSigma, Burlington, MA), and 100 µg/mL carbenicillin (Gold Biotechnology, Olivette, MO). Plates were incubated overnight at 30 °C. Single colonies were selected and cultured in 3 mL of LB Miller broth containing the same concentrations of glucose and antibiotics in 24-deep-well plates (Thermo Fisher Scientific, Waltham,

MA) at 30 °C for 16 hours with shaking at 600 rpm on a microplate incubator (Incu-mixer™ MP Heated Microplate Vortexer; Benchmark Scientific Inc, Sayreville, NJ). For GV expression, overnight cultures were diluted to an initial optical density at 600 nm (OD_{600}) of 0.05 in 3 mL of 2×YT (2× Yeast Extract Tryptone medium) broth (Thermo Fisher Scientific, Waltham, MA) with 0.2% glucose, 25 µg/mL chloramphenicol (MilliporeSigma, Burlington, MA), and 100 µg/mL carbenicillin (Gold Biotechnology, Olivette, MO) within 24-deep-well plates. All cell cultures were incubated at 30°C with shaking at 600 rpm until an OD_{600} of 0.6–0.8 was reached. For cells with the wild-type pNL29 plasmid, isopropyl β-D-1-thiogalactopyranoside (IPTG; Teknova, Hollister, CA) was added to final concentrations of 0, 20, 200, or 400 µM to induce expression. For cells with dual-inducer transcriptional regulation system variants plasmids, induction was performed with either IPTG or anhydrotetracycline (aTc; MilliporeSigma, Burlington, MA) with concentrations specified in the figure legends following the same OD_{600} threshold. After an additional 3 hours of incubation under the same conditions, a second inducer (IPTG or aTc) was added as per experimental design.

150 µL of culture was transferred into wells of the 96-well black, flat-bottom polystyrene microplate (Corning® 96-well Black Flat Bottom Polystyrene Not Treated Microplate 3631; Corning Inc., Corning, NY) for each measurement. Cell growth was tracked by measuring OD_{600} using the TECAN Spark multimode microplate reader (Tecan Group Ltd., Männedorf, Switzerland) with software SparkControl™ (version 3.1.10).

Isolation, purification, and quantification of GVs

E. coli cultures expressing GVs were harvested and subjected to low-speed centrifugation to exploit the buoyant properties of GVs. Cultures were centrifuged at $400 \times g$ for 4 hours at 4 °C in 2.0 mL Eppendorf™ Safe-Lock tubes (Thermo Fisher Scientific, Waltham, MA), with a sample volume of 1.5 mL per tube. The intermediate layer between the buoyant GV-containing fraction and the sedimented cells was carefully removed using a syringe. The remaining cell pellet was resuspended in SoluLyse-Tris buffer (Genlantis, San Diego, CA) at a volume of 60 µL per 1.5 mL of initial culture. Lysozyme (MilliporeSigma, Burlington, MA) and RNase-free Deoxyribonuclease I (DNase I; MilliporeSigma, Burlington, MA) were added to final concentrations of 250 µg/mL and 10 µg/mL, respectively, to facilitate cell lysis and nucleic acid degradation. The suspension was incubated with gentle rotation at 4 °C for 30 minutes. Post-lysis, the samples underwent a second centrifugation at $400 \times g$ for 2 hours at 4 °C to separate the buoyant GVs from cellular debris, as depicted in **Fig. 8e**. The buoyant GVs accumulated at the top of the liquid surface were carefully collected by aspirating the underlying supernatant and cell debris using a syringe. The isolated GVs were subjected to three successive washes with 1× PBS (Teknova, Hollister, CA), each followed by centrifugation under the same conditions.

Purified GV samples were standardized to a final volume of 1.5 mL by resuspension in 1× PBS. The OD_{500} was measured using a Take3 microvolume plate on an Agilent BioTek Synergy H4 Hybrid microplate reader (Agilent Technologies, Santa Clara, CA). The measured OD_{500} values were normalized by dividing by the corresponding OD_{600} of the *E. coli* cultures before lysis to account for variations in cell density at the time of harvest.

Bacterial viability quantification via flow cytometry

Cell viability was assessed by flow cytometry using a Sony SA3800 spectral cell analyzer and a standard Live/Dead assay. *E. coli* cultures were harvested at predetermined time points and pelleted by low-speed centrifugation (400× g). Cell pellets were resuspended and stained with 5 µM SYTO 9 (Invitrogen,

Waltham, MA) and 50 µg/mL propidium iodide (PI; Invitrogen, Waltham, MA), followed by incubation for 15 min at 4 °C in the dark.

During data acquisition, all parameters were collected in logarithmic mode. The gating strategy was shown in **Supplementary Fig. 15**. Data were analyzed using FlowJo™ v10.8 software (BD Life Sciences, Franklin Lakes, NJ). Forward and side scatter gating were applied to exclude debris and doublets. Unstained samples, untreated live cultures, and 70% isopropanol-treated dead cultures served as controls for gate definition. Flow cytometry figures were generated in R (R version 4.5.1) using the packages *flowCore*, *ggplot2*, and *hexbin*⁷³.

Colony-forming unit (CFU) assay for cell viability

Cell viability was also determined by colony-forming unit (CFU) assays. At specified time points after induction, 200 µL of culture was withdrawn from each condition and serially diluted in sterile 1× PBS to final dilutions of 10⁵–10⁷, depending on culture density. Aliquots of 50 µL from each dilution were spread onto LB Miller agar plates (Thermo Fisher Scientific, Waltham, MA) with 0.2% glucose, 25 µg/mL chloramphenicol (MilliporeSigma, Burlington, MA), and 100 µg/mL carbenicillin (Gold Biotechnology, Olivette, MO). Plates were then incubated at 37 °C for 24 h, and colonies were counted using a semi-automatic colony counter.

The CFU per milliliter of the original culture was calculated using the equation: CFU/mL = $N \times D / V$, where N is the number of colonies counted on the plate, D is the dilution factor, and V is the volume plated in mL. Only plates yielding 30–300 colonies were used for CFU/mL calculations to ensure statistical accuracy and reproducibility.

Fluorescent reporter protein expression in *E. coli*

Plasmids encoding either dual-inducer transcriptional regulation system variants or single-reporter constructs were transformed into chemically competent *E. coli* cells using standard heat-shock protocols, as mentioned in the previous section. Following transformation, cells were incubated and cultured under the conditions described in the previous section. Upon reaching OD₆₀₀ of 0.6–0.8, induction strategies were applied according to the experimental designs outlined in **Fig. 3** and **Supplementary Fig. 5–7**.

Fluorescence intensity measurements of *E. coli* cultures expressing fluorescent reporter proteins were conducted using a multimode microplate reader. A volume of 150 µL from each culture was transferred into individual wells of a 96-well black, flat-bottom polystyrene microplate (Corning® 96-well Black Flat Bottom Polystyrene Not Treated Microplate 3631; Corning Inc., Corning, NY). For mCherry fluorescence detection, the excitation wavelength was set at 587 nm, and the emission was detected at 610 nm, with a bandwidth of 5 nm. For sfGFP fluorescence detection, the excitation wavelength was 488 nm, and the emission wavelength was 510 nm, with a bandwidth of 5 nm. Gain settings were optimized to 150 for both to ensure signal linearity and prevent detector saturation. All measurements were performed at room temperature, and data acquisition was managed using the SparkControl software (version 3.1 SP1). Fold change in fluorescence intensity values in **Fig. 3** and **Supplementary Fig. 5–7** were calculated using the equation: Fold change in fluorescence intensity = [(measured fluorescence intensity of studied cells) / (OD₆₀₀ of culture at harvest of studied cells)] / [(measured fluorescence intensity of not induced cells) / (OD₆₀₀ of culture at harvest of not induced cells)].

Temporal induction of assembly factors protein and shell protein in *E. coli*

Transformation of plasmids into chemically competent *E. coli* cells, subsequent incubation, and GV expression were performed following the protocols and conditions described in previous sections. Various induction strategies were implemented based on the experimental design. In the "IPTG (start)" condition (**Fig. 9**), IPTG (Teknova, Hollister, CA) was added at the initiation of culture, and aTc (MilliporeSigma, Burlington, MA) was introduced when cultures reached OD₆₀₀ of 0.6–0.8. For the "aTc (-2 h)" and "aTc (-1 h)" conditions (**Fig. 9**), aTc was administered 2 hours and 1 hour, respectively, before IPTG induction at OD₆₀₀ of 0.6–0.8. In the "aTc (0 h)" condition (**Fig. 9**), both IPTG and aTc were simultaneously added upon cultures reaching OD₆₀₀ of 0.6–0.8. Additional induction schemes (**Fig. 9**), labeled as "aTc (x h)," involved the addition of aTc at defined time intervals (x hours) following IPTG induction at OD₆₀₀ of 0.6–0.8. Following induction, GVs were purified from each experimental group and quantified using the previously described protocols.

Transmission electron microscopy

E. coli cell samples were diluted to OD₆₀₀ of 0.1 in 1× PBS. A 5 µL aliquot of the diluted suspension was applied to a 200-mesh carbon-coated copper grid (Ted Pella) and incubated for 3 minutes to allow adherence. Excess liquid was gently removed by blotting with Whatman filter paper (MilliporeSigma, Burlington, MA). For negative staining of purified GVs, samples were diluted to OD₅₀₀ of 0.2 in 1× PBS. A 5 µL aliquot of the diluted sample was applied to a 200-mesh carbon-coated copper grid (Ted Pella, Redding, CA) and incubated for 3 minutes. Excess liquid was carefully blotted away using Whatman filter paper (MilliporeSigma, Burlington, MA). Subsequently, the grids were stained with a 5 µL drop of 2% (w/v) uranyl acetate solution (Electron Microscopy Sciences, Hatfield, PA) for contrast enhancement. After staining, excess stain was removed by blotting with filter paper. The grids were then air-dried in a chemical fume hood with lateral ventilation for 2 hours to ensure complete drying. High-resolution TEM imaging was performed using a JEOL JEM-2100 Field Emission Gun TEM and an FEI Tecnai F20 TEM.

Hydrostatic collapse assay

The experimental setup for hydrostatic collapse assay with pressurized absorbance spectroscopy was configured as previously described³⁸. The system comprised (**Fig. 7a**): (1) a computer running MATLAB scripts to control pressure application; (2) a compressed nitrogen gas cylinder equipped with control valves and a pressure regulator; (3) a single-valve pressure controller (PC series; Alicat Scientific, Tucson, AZ) interfaced with the computer; (4) a quartz cuvette (176.700-QS; Hellma GmbH & Co. KG, Müllheim, Germany); and (5) a UV–Vis spectrophotometer (STS-VIS; Ocean Optics, Orlando, FL) with an integrated light source and cuvette holder. Purified GVs were diluted to OD₅₀₀ of 0.2 in 1× PBS. *E. coli* cells expressing GVs and other GV variants were lysed following the protocol detailed in the previous section and treated with 6 M urea. Samples were loaded into a pressurizable cuvette. OD₅₀₀ was measured using the spectrophotometer, while the cuvette was subjected to increasing pressure via a single-valve pressure controller. The pressure was incrementally increased from 0 to 1.4 MPa in 0.2 MPa steps, allowing for the assessment of GV collapse under controlled hydrostatic pressure conditions.

OD₅₀₀ were normalized using the following equation: Normalized OD₅₀₀ = (Measured OD₅₀₀ - Minimum OD₅₀₀) / (Maximum OD₅₀₀ - Minimum OD₅₀₀). Hydrostatic collapse profiles were fitted using a Boltzmann sigmoidal function, with constraints set such that the bottom equals 0 and the top equals 1, to model the transition from intact to collapsed states. A coefficient of determination (*R*²) of this nonlinear fit was provided. To quantify GV expression levels in *E. coli* while accounting for variations in cell density, we normalized the reduction in OD₅₀₀, calculated as follows: Normalized reduction in OD₅₀₀ = (Maximum

$\text{OD}_{500} - \text{Minimum OD}_{500}) / \text{OD}_{600}$ at harvest. This metric provides a standardized measure of GV production per unit of cellular biomass.

***In vitro* protein synthesis**

GvpA2 and GvpA2::His₆-tag proteins were synthesized *in vitro* using the PURExpress® *In Vitro* Protein Synthesis Kit (New England Biolabs, Ipswich, MA), following the manufacturer's protocol. Each 25 µL reaction was assembled on ice, comprising 10 µL of Solution A, 7.5 µL of Solution B, 0.5 µL of Murine RNase Inhibitor (40 U/µL; New England Biolabs), 5 µL of nuclease-free water, and 2 µL of 125 ng/µL plasmid DNA encoding dihydrofolate reductase (DHFR) control, GvpA2 under the control of a T7 promoter. 2 µL of nuclease-free water was added as a no plasmid control. The reaction mixtures were gently mixed by pipetting and incubated at 37 °C for 2 hours to facilitate coupled transcription-translation. After incubation, reactions were placed on ice to halt protein synthesis.

Live-cell fluorescence and phase contrast microscopy

E. coli cells expressing mCherry, mCherry::GvpA2, or GvpA2::mCherry were grown under conditions previously described. 4 hours post-induction with IPTG cells were pelleted by centrifugation and washed three times with Hank's Balanced Salt Solution (HBSS; Thermo Fisher Scientific, Waltham, MA). The cell suspension was then diluted in HBSS and applied to 35 mm glass-bottom dishes with number 1.5 coverslips (MatTek Life Sciences, Ashland, MA) for imaging. Live-cell fluorescence imaging was performed using a ZEISS Elyra 7 microscope (Carl Zeiss AG, Germany) equipped with SIM² Lattice Structured Illumination Microscopy (SIM) and Total Internal Reflection Fluorescence (TIRF) capabilities. The system was configured with a Plan-Apochromat 63×/1.46 oil immersion objective lens. mCherry fluorescence signal was excited using a 561 nm laser line, and emission was collected between 580–620 nm using a PCO.edge sCMOS camera. Image acquisition and processing were performed using ZEISS ZEN Blue (version 3.11) and Fiji (ImageJ2).

In vitro protein synthesis reactions were analyzed using phase contrast microscopy to assess sample morphology. A 5 µL aliquot of each reaction mixture was applied to a 35 mm glass-bottom dish with a No. 1.5 coverslip (MatTek Life Sciences, Ashland, MA). Imaging was acquired on a Nikon Eclipse Ti2 microscope (Nikon, Japan) equipped with a 40×/0.60 NA objective lens and a phase contrast ring corresponding to Ph2. The microscope was configured for Köhler illumination, and phase contrast images were captured using a PCO.edge sCMOS camera. Image acquisition and processing were conducted using Nikon NIS-Elements software (version 6.10. 01) and Fiji (ImageJ2).

Quantification and statistical analysis

The figures and figure captions provide details regarding biologically independent sample size (*n*), *P*-values, and other statistical information. All statistical analyses were conducted using GraphPad Prism software (version 10.4.2). Data are presented as mean ± standard deviation (s.d.). Comparisons between two groups were evaluated using a two-tailed unpaired Student's *t*-test with Welch's correction to account for unequal variances. For multiple group comparisons, the Brown–Forsythe and Welch one-way analysis of variance (ANOVA) with Dunnett's T3 correction was employed, which does not assume equal variance across groups. Statistical significance was defined as *P* < 0.05.

Statistics and reproducibility

All representative micrographs are based on experiments repeated independently at least three times (*n* = 3 biologically independent samples).

ARTICLE IN PRESS

ARTICLE IN PRESS

Data availability

All data generated in this study are included in the Source Data file provided with this paper.

Reference

1. Vincent, R.L. *et al.* Probiotic-guided CAR-T cells for solid tumor targeting. *Science* **382**, 211–218 (2023).
2. Gurbatri, C.R. *et al.* Engineered probiotics for local tumor delivery of checkpoint blockade nanobodies. *Science translational medicine* **12**, eaax0876 (2020).
3. Ke, J., Wang, B. & Yoshikuni, Y. Microbiome engineering: synthetic biology of plant-associated microbiomes in sustainable agriculture. *Trends in Biotechnology* **39**, 244–261 (2021).
4. Gootenberg, J.S. *et al.* Nucleic acid detection with CRISPR-Cas13a/C2c2. *Science* **356**, 438–442 (2017).
5. Levskaya, A. *et al.* Engineering Escherichia coli to see light. *Nature* **438**, 441–442 (2005).
6. Konermann, S. *et al.* Optical control of mammalian endogenous transcription and epigenetic states. *Nature* **500**, 472–476 (2013).
7. Roybal, K.T. *et al.* Engineering T Cells with Customized Therapeutic Response Programs Using Synthetic Notch Receptors. *Cell* **167**, 419–432.e416 (2016).
8. Schmidt, F. *et al.* Noninvasive assessment of gut function using transcriptional recording sentinel cells. *Science* **376**, eabm6038 (2022).
9. Din, M.O. *et al.* Synchronized cycles of bacterial lysis for in vivo delivery. *Nature* **536**, 81–85 (2016).
10. Dahl, R.H. *et al.* Engineering dynamic pathway regulation using stress-response promoters. *Nature biotechnology* **31**, 1039–1046 (2013).
11. Ceroni, F. *et al.* Burden-driven feedback control of gene expression. *Nature Methods* **15**, 387–393 (2018).
12. Wu, G. *et al.* Metabolic burden: cornerstones in synthetic biology and metabolic engineering applications. *Trends in biotechnology* **34**, 652–664 (2016).
13. Way, J.C., Collins, J.J., Keasling, J.D. & Silver, P.A. Integrating biological redesign: where synthetic biology came from and where it needs to go. *Cell* **157**, 151–161 (2014).
14. Rodrigo-Navarro, A., Sankaran, S., Dalby, M.J., del Campo, A. & Salmeron-Sanchez, M. Engineered living biomaterials. *Nature Reviews Materials* **6**, 1175–1190 (2021).
15. Zhou, S., Gravekamp, C., Bermudes, D. & Liu, K. Tumour-targeting bacteria engineered to fight cancer. *Nature Reviews Cancer* **18**, 727–743 (2018).
16. Sørensen, S.J., Bailey, M., Hansen, L.H., Kroer, N. & Wuertz, S. Studying plasmid horizontal transfer in situ: a critical review. *Nature Reviews Microbiology* **3**, 700–710 (2005).
17. Bourdeau, R.W. *et al.* Acoustic reporter genes for noninvasive imaging of microorganisms in mammalian hosts. *Nature* **553**, 86–90 (2018).

18. Farhadi, A., Ho, G.H., Sawyer, D.P., Bourdeau, R.W. & Shapiro, M.G. Ultrasound imaging of gene expression in mammalian cells. *Science* **365**, 1469–1475 (2019).
19. Pfeifer, F. Distribution, formation and regulation of gas vesicles. *Nat Rev Microbiol* **10**, 705–715 (2012).
20. Walsby, A.E. Gas vesicles. *Microbiol Rev* **58**, 94–144 (1994).
21. Walsby, A.E. & Hayes, P.K. Gas vesicle proteins. *Biochemical Journal* **264**, 313 (1989).
22. Shapiro, M.G. *et al.* Biogenic gas nanostructures as ultrasonic molecular reporters. *Nature Nanotechnology* **9**, 311–316 (2014).
23. Shapiro, M.G. *et al.* Genetically encoded reporters for hyperpolarized xenon magnetic resonance imaging. *Nat Chem* **6**, 630–635 (2014).
24. Bar-Zion, A. *et al.* Acoustically triggered mechanotherapy using genetically encoded gas vesicles. *Nature Nanotechnology* **16**, 1403–1412 (2021).
25. Wu, D. *et al.* Biomolecular actuators for genetically selective acoustic manipulation of cells. *Sci Adv* **9** (2023).
26. Yang, Y. *et al.* In-vivo programmable acoustic manipulation of genetically engineered bacteria. *Nature Communications* **14**, 3297 (2023).
27. Anthis, A.H.C. *et al.* Modular stimuli-responsive hydrogel sealants for early gastrointestinal leak detection and containment. *Nature Communications* **13** (2022).
28. Shen, Q. *et al.* 50-nm Gas-Filled Protein Nanostructures to Enable the Access of Lymphatic Cells by Ultrasound Technologies. *Adv Mater* **36**, e2307123 (2024).
29. Ling, B. *et al.* Truly Tiny Acoustic Biomolecules for Ultrasound Imaging and Therapy. *Adv Mater* **36**, e2307106 (2024).
30. Xie, L., Wang, J., Song, L., Jiang, T. & Yan, F. Cell-cycle dependent nuclear gene delivery enhances the effects of E-cadherin against tumor invasion and metastasis. *Signal Transduct Target Ther* **8**, 182 (2023).
31. Lakshmanan, A. *et al.* Acoustic biosensors for ultrasound imaging of enzyme activity. *Nature Chemical Biology* **16**, 988–996 (2020).
32. Jin, Z. *et al.* Ultrasonic reporters of calcium for deep tissue imaging of cellular signals. *bioRxiv*, 2023.2011.2009.566364 (2023).
33. Huber, S.T., Terwiel, D., Evers, W.H., Maresca, D. & Jakobi, A.J. Cryo-EM structure of gas vesicles for buoyancy-controlled motility. *Cell* **186**, 975–986 e913 (2023).
34. Dutka, P. *et al.* Structure of *Anabaena flos-aquae* gas vesicles revealed by cryo-ET. *Structure* **31**, 518–528 e516 (2023).
35. Iburg, M. *et al.* Elucidating the assembly of gas vesicles by systematic protein-protein interaction analysis. *EMBO J* **43**, 4156–4172 (2024).

36. Li, N. & Cannon, M.C. Gas vesicle genes identified in *Bacillus megaterium* and functional expression in *Escherichia coli*. *J Bacteriol* **180**, 2450–2458 (1998).
37. Li, Z. *et al.* Phase transition of GvpU regulates gas vesicle clustering in bacteria. *Nature Microbiology* **9**, 1021–1035 (2024).
38. Lakshmanan, A. *et al.* Preparation of biogenic gas vesicle nanostructures for use as contrast agents for ultrasound and MRI. *Nat Protoc* **12**, 2050–2080 (2017).
39. Stiefel, P., Schmidt-Emrich, S., Maniura-Weber, K. & Ren, Q. Critical aspects of using bacterial cell viability assays with the fluorophores SYTO9 and propidium iodide. *BMC microbiology* **15**, 36 (2015).
40. Pfeifer, F. Recent Advances in the Study of Gas Vesicle Proteins and Application of Gas Vesicles in Biomedical Research. *Life (Basel)* **12** (2022).
41. Jung, H. *et al.* Heterologous expression of cyanobacterial gas vesicle proteins in *Saccharomyces cerevisiae*. *Biotechnology Journal* **16**, 2100059 (2021).
42. Tyedmers, J., Mogk, A. & Bukau, B. Cellular strategies for controlling protein aggregation. *Nature reviews Molecular cell biology* **11**, 777–788 (2010).
43. Rosano, G.L. & Ceccarelli, E.A. Recombinant protein expression in *Escherichia coli*: advances and challenges. *Frontiers in microbiology* **5**, 172 (2014).
44. Hofacker, A., Schmitz, K.M., Cichonczyk, A., Sartorius-Neef, S. & Pfeifer, F. GvpE- and GvpD-mediated transcription regulation of the p-gvp genes encoding gas vesicles in *Halobacterium salinarum*. *Microbiology (Reading)* **150**, 1829–1838 (2004).
45. Lorenzetti, A.P. *et al.* A genome-scale atlas reveals complex interplay of transcription and translation in an archaeon. *Msystems* **8**, e00816–00822 (2023).
46. Zimmermann, P. & Pfeifer, F. Regulation of the expression of gas vesicle genes in *Haloferax mediterranei*: interaction of the two regulatory proteins GvpD and GvpE. *Molecular microbiology* **49**, 783–794 (2003).
47. Lutz, R. & Bujard, H. Independent and tight regulation of transcriptional units in *Escherichia coli* via the LacR/O, the TetR/O and AraC/I1-I2 regulatory elements. *Nucleic acids research* **25**, 1203–1210 (1997).
48. Darlington, A.P., Kim, J., Jiménez, J.I. & Bates, D.G. Dynamic allocation of orthogonal ribosomes facilitates uncoupling of co-expressed genes. *Nature communications* **9**, 695 (2018).
49. Studier, F.W. & Moffatt, B.A. Use of bacteriophage T7 RNA polymerase to direct selective high-level expression of cloned genes. *Journal of molecular biology* **189**, 113–130 (1986).
50. Gossen, M. & Bujard, H. Tight control of gene expression in mammalian cells by tetracycline-responsive promoters. *Proceedings of the National Academy of Sciences* **89**, 5547–5551 (1992).
51. Chamberlin, M., McGrath, J. & Waskell, L. New RNA polymerase from *Escherichia coli* infected with

- bacteriophage T7. *Nature* **228**, 227–231 (1970).
52. Hurt, R.C. *et al.* Genomically mined acoustic reporter genes for real-time in vivo monitoring of tumors and tumor-homing bacteria. *Nature Biotechnology* **41**, 919–931 (2023).
53. Hurt, R.C. *et al.* Directed Evolution of Acoustic Reporter Genes Using High-Throughput Acoustic Screening. *ACS Synthetic Biology* **13**, 2215–2226 (2024).
54. Dyer, S.W. & Needoba, J.A. Use of High-Resolution Pressure Nephelometry To Measure Gas Vesicle Collapse as a Means of Determining Growth and Turgor Changes in Planktonic Cyanobacteria. *Applied and Environmental Microbiology* **86**, e01790–01719 (2020).
55. Tavlaridou, S., Faist, K., Weitzel, K. & Pfeifer, F. Effect of an overproduction of accessory Gvp proteins on gas vesicle formation in *Haloferax volcanii*. *Extremophiles* **17**, 277–287 (2013).
56. Scott, M., Gunderson, C.W., Mateescu, E.M., Zhang, Z. & Hwa, T. Interdependence of cell growth and gene expression: origins and consequences. *Science* **330**, 1099–1102 (2010).
57. Bashor, C.J., Hilton, I.B., Bandukwala, H., Smith, D.M. & Veiseh, O. Engineering the next generation of cell-based therapeutics. *Nature Reviews Drug Discovery* **21**, 655–675 (2022).
58. Meyer, A.J., Segall-Shapiro, T.H., Glassey, E., Zhang, J. & Voigt, C.A. Escherichia coli “Marionette” strains with 12 highly optimized small-molecule sensors. *Nature Chemical Biology* **15**, 196–204 (2019).
59. Rouches, M.V., Xu, Y., Cortes, L.B.G. & Lambert, G. A plasmid system with tunable copy number. *Nature Communications* **13**, 3908 (2022).
60. Toettcher, J.E., Weiner, O.D. & Lim, W.A. Using optogenetics to interrogate the dynamic control of signal transmission by the Ras/Erk module. *Cell* **155**, 1422–1434 (2013).
61. Völkner, K., Jost, A. & Pfeifer, F. Accessory Gvp proteins form a complex during gas vesicle formation of haloarchaea. *Frontiers in microbiology* **11**, 610179 (2020).
62. Jost, A. & Pfeifer, F. Interaction of the gas vesicle proteins GvpA, GvpC, GvpN, and GvpO of *Halobacterium salinarum*. *Frontiers in Microbiology* **13**, 971917 (2022).
63. Mutualik, V.K. *et al.* Precise and reliable gene expression via standard transcription and translation initiation elements. *Nature methods* **10**, 354–360 (2013).
64. Silva-Rocha, R. *et al.* The Standard European Vector Architecture (SEVA): a coherent platform for the analysis and deployment of complex prokaryotic phenotypes. *Nucleic acids research* **41**, D666–D675 (2013).
65. Nishihara, K., Kanemori, M., Kitagawa, M., Yanagi, H. & Yura, T. Chaperone coexpression plasmids: differential and synergistic roles of DnaK-DnaJ-GrpE and GroEL-GroES in assisting folding of an allergen of Japanese cedar pollen, Cryj2, in *Escherichia coli*. *Applied and environmental microbiology* **64**, 1694–1699 (1998).
66. Shiloach, J. & Fass, R. Growing *E. coli* to high cell density—a historical perspective on method

- development. *Biotechnology advances* **23**, 345–357 (2005).
67. Kerfeld, C.A., Aussignargues, C., Zarzycki, J., Cai, F. & Sutter, M. Bacterial microcompartments. *Nature Reviews Microbiology* **16**, 277–290 (2018).
68. Li, P. *et al.* Phase transitions in the assembly of multivalent signalling proteins. *Nature* **483**, 336–340 (2012).
69. Zhang, F. *et al.* Independent control of amplitude and period in a synthetic oscillator circuit with modified repressilator. *Communications Biology* **5**, 23 (2022).
70. Brandman, O., Ferrell, J.E., Li, R. & Meyer, T. Interlinked Fast and Slow Positive Feedback Loops Drive Reliable Cell Decisions. *Science* **310**, 496–498 (2005).
71. Gardner, T.S., Cantor, C.R. & Collins, J.J. Construction of a genetic toggle switch in Escherichia coli. *Nature* **403**, 339–342 (2000).
72. Meng, E.C. *et al.* UCSF ChimeraX: Tools for structure building and analysis. *Protein Science* **32**, e4792 (2023).
73. Hahne, F. *et al.* flowCore: a Bioconductor package for high throughput flow cytometry. *BMC bioinformatics* **10**, 106 (2009).

Acknowledgments

We thank the Shared Equipment Authority (SEA) at Rice University for access to core facilities and instrumentation, and Dr. Wenhua Guo and Dr. Alloysius Budi Utama for technical training. This work was supported by the Cancer Prevention and Research Institute of Texas (CPRIT, RR190081), the National Institutes of Health (NIH, R35GM155015 and R21EB033607), the Welch Foundation (C-2249 and C-2069), the G. Harold and Leila Y. Mathers Foundation, the John S. Dunn Foundation, and the Open Collective Foundation.

Author Contributions

Conceptualization, G.J.L., Z.L., C.Y.H; Methodology, G.J.L., Z.L., C.Y.H, S.J., L.M.; Investigation, Z.L., C.Y.H, D.B., S.J.; Formal Analysis, Z.L., C.Y.H, D.B., S.J.; Manuscript writing, G.J.L., Z.L., C.Y.H, S.J.; Supervision and Funding Acquisition, G.J.L. All authors have reviewed and approved the final version of the manuscript.

Competing interests

The authors declare no competing interests.

Fig. 1 | Heterologous expression of the GVs impaired bacterial growth.

a, Schematic representation of the plasmid containing the pNL29 operon architecture.

b, Representative TEM images of wild-type pNL29 GVs with 6 M urea treatment applied to uncluster these GVs after purification.

c, Schematic representation of pNL29 GVs expression in *E. coli*.

d, Growth profiles of *E. coli* expressing wild-type pNL29 GVs or MBP after induction with 20 μ M IPTG, monitored by optical density at 600 nm (Measured OD₆₀₀). Data represent mean \pm standard deviation (s.d.) ($n = 6$ biologically independent samples). Absorbance (y-axis) is reported in absorbance units (AU), representing the amount of light absorbed by the culture at 600 nm wavelength.

e, Representative TEM images depicting an intact *E. coli* cell expressing wild-type pNL29 GVs at 4 h post-induction (grey) and a lysed *E. coli* cell illustrating the release of GVs at 8 h post-induction (red).

f, Representative colony formation assay plates used for CFU quantification of *E. coli* cultures expressing MBP control or wild-type pNL29 GVs. Additional representative plates are shown in **Supplementary Fig. 3a, c.**

g, CFU measurements of *E. coli* cultures expressing wild-type pNL29 GVs or MBP control under 20 μ M IPTG induction. CFU/mL was quantified over 24 h, with data points representing mean \pm standard deviation (s.d.) from $n = 3$ biologically independent samples for both groups.

h, Representative SYTO9/PI flow-cytometry plots of *E. coli* expressing wild-type pNL29 GVs or MBP control under 20 μ M IPTG. Samples were taken at 0, 4, 8, 12, and 24 h post-induction. The red dashed gate marks PI-positive (dead) cells; values indicate their percentage of the total population. Additional plots are shown in **Supplementary Fig. 3e**.

i, Cell viability of *E. coli* expressing wild-type pNL29 GVs or MBP control under 20 μ M IPTG, quantified from flow cytometry (mean \pm s.d., $n = 3$ biological replicates). Two-tailed paired Student's *t*-test: NS ($P > 0.05$) at 0 h; $P = 0.0452$, 0.0001, 0.0012, and 0.0016 at 4, 8, 12, and 24 h post-induction.

Scale bars, 500 nm in **b**, **e**, and 20 mm in **f**.

ARTICLE IN PRESS

ARTICLE IN PRESS

Fig. 2 | Hydrophobic shell protein GvpA2 forms aggregates in cells and *in vitro*, and triggers proteotoxic stress in heterologous expression

a, Amino acid sequence and cryo-EM structure³³ (PDB 7R1C) of the major gas vesicle shell protein GvpA2. Structural segments are annotated as N-terminal (Nt), first α -helix (α_1), first β -sheet (β_1), second β -sheet (β_2), second α -helix (α_2), and C-terminal (Ct) regions. Hydrophobic residues are depicted in yellow, while hydrophilic residues are shown in light blue.

b, Structural organization of GvpA2 within the GV shell (PDB 7R1C). Hydrophobic amino acid residues of GvpA2 are oriented toward the GV's interior, establishing a gas-facing surface, while hydrophilic residues are exposed on the exterior, interfacing with the aqueous environment.

c, Growth profiles of *E. coli* with mean \pm s.d. for $n = 6$ biologically independent samples for the GvpA2-expressing cultures and MBP-expressing cultures. Absorbance (y-axis) is reported in absorbance units (AU).

d, CFU/mL of *E. coli* expressing GvpA2 or MBP under 20 μ M IPTG, quantified over 24 h (mean \pm s.d., $n = 3$ biological replicates). The light-purple inset shows representative GvpA2 plates at 4 h (1:10⁷ for 0 and 20 μ M IPTG; 1:10⁵ for 20 μ M), illustrating reduced viable counts. Additional representative plates are shown in **Supplementary Fig. 4a**.

e, Cell viability of *E. coli* expressing GvpA2 or MBP under 20 μ M IPTG, quantified by SYTO9/PI flow cytometry (mean \pm s.d., $n = 3$ biological replicates). Two-tailed paired Student's t-test: NS at 0, 12, and 24 h; $P = 0.0229$ at 4 h and < 0.0001 at 8 h. Insets show representative GvpA2 plots at 4 and 8 h with red gates marking PI-positive cells. Additional representative plots are shown in **Supplementary Fig. 4c**.

f, Fluorescence microscopy images of *E. coli* cells expressing mCherry, mCherry::GvpA2, and GvpA2::mCherry.

g, Fluorescence microscopy images of *E. coli* cells expressing mCherry with its C-terminus fused to defined segments of GvpA2. Structural annotations on the right corners of micrographs correspond to those shown in **a**.

Scale bars, 20 mm in **d** and 2 μ m in **f** and **g**.

ARTICLE IN PRESS

ARTICLE IN PRESS

Fig. 3 | Dual-inducer transcriptional regulation enabling independent control of assembly factor and shell protein expression.

a, Schematic representation of the gas vesicle (gvp) gene clusters in *Halobacterium salinarum* (*Hbt. salinarum*). The regulatory genes *gvpD* and *gvpE* are transcribed in opposite orientations within the cluster. GvpE (blue) functions as a transcriptional activator, enhancing the expression of structural gvp genes, while GvpD (purple) acts as a repressor by reducing the intracellular levels of GvpE, thereby modulating GV formation in *Hbt. salinarum*.

b, Schematic representation of the dual-inducer transcriptional regulation system designed for independent control of assembly factor proteins and shell protein expression. Assembly protein genes are placed under the control of a T7 promoter, with transcription initiated by T7 RNA polymerase expression upon induction with IPTG (purple). Shell protein gene expression is regulated by a tetracycline-responsive promoter (aTc-inducible system), where transcription is repressed by the Tet repressor (TetR) in the absence of aTc and derepressed upon aTc addition (yellow).

ARTICLE IN PRESS

ARTICLE IN PRESS

Fig. 4 | Fluorescent reporter analysis demonstrating low basal expression and minimal regulatory crosstalk in the dual-inducer system.

a, b, Schematic representation of the genetic constructs of the dual-inducer system (**a**) and two single-reporter constructs (**b**) for fluorescent reporter proteins expression.

c, d, Fluorescence fold change of dual-inducer vs. single-reporter across inducer concentrations. (**c**) mCherry-only vs. mCherry-dual: NS at 0 μ M IPTG; $P = 0.0003$, < 0.0001 ($P = 0.00000058$), and < 0.0001 ($P = 0.000003$) at 20, 200, and 400 μ M. (**d**) sfGFP-only vs. sfGFP-dual: NS for all.

e, f, Fluorescence fold change of the dual-inducer vs. single-reporter without the corresponding inducer. (**e**) mCherry-dual vs. mCherry-only. $P = 0.00461$, 0.0165 , < 0.0001 ($P = 0.00002$) at 0, 50, 500 ng/mL aTc. NS at 1000 ng/mL. (**f**) sfGFP-dual vs. sfGFP-only. NS at 0, 20, 200 μ M IPTG; $P = 0.00461$ at 400 μ M.

g, j, Schematic representation of the dual-inducer system induced with varying concentrations of IPTG at fixed aTc concentration (**g**) or with varying concentrations of aTc at fixed IPTG concentration (**j**).

h, k, Fold change in mCherry (**h**) and sfGFP (**k**). mCherry: 0 vs. 500 ng/mL aTc across IPTG concentrations: NS at 0, 20 μ M; $P = 0.0238$, 0.0044 at 200, 400 μ M. sfGFP: 0 vs. 200 μ M IPTG across aTc concentrations: NS at 0, 50 ng/mL; $P = 0.0089$, 0.0012 at 500, 1000 ng/mL.

i, l, Fold change in sfGFP (**i**) and mCherry (**l**). (**i**) sfGFP-dual cultures at 500 ng/mL aTc without IPTG vs. 0–400 μ M IPTG: NS at 0 μ M; $P = 0.0009$, 0.0007 , 0.0010 at 20, 200, 400 μ M. (**l**) mCherry-dual cultures at 200 μ M IPTG without aTc vs. 0–1000 ng/mL aTc: NS at 0ng/mL; $P = 0.0478$, 0.0013 , 0.0145 at 50, 500, 1000 ng/mL.

Fold change in **c, d, e, f, h, i, k**, and **l** is plotted in arbitrary units (AU, y-axis), data representing mean \pm s.d. ($n = 6$ biologically independent samples). Statistics: **c, d, h, k** by two-tailed unpaired Welch *t*-test; **e, f, i, l** vs. grey controls by Brown–Forsythe and Welch one-way ANOVA with Dunnett T3 correction.

ARTICLE IN PRESS

ARTICLE IN PRESS

Fig. 5 | Sequential expression of assembly factor proteins prior to shell protein synthesis mitigates proteotoxic stress and restores normal growth in *E. coli*.

a, b, Schematic representation of the genetic construct for GV expression under the dual-inducer system. Cultures were induced with varying concentrations of IPTG while maintaining a constant aTc concentration (**a**) or induced with varying concentrations of aTc while maintaining a constant IPTG concentration (**b**).

c, d, Growth profiles of *E. coli* cultures expressing GVs under the dual-inducer system with inducing strategies in **a** (**c**) and **b** (**d**). The growth profile of wild-type pNL29 GV-operon-expressing *E. coli* cultures induced with 20 µM IPTG (WT) served as the control. The vertical grey dashed line indicates the time point at which aTc was introduced. The horizontal black dashed line indicates the average OD₆₀₀ value of the MBP control from **Fig. 1d** and **Fig. 2c** at 24 h post-induction, representing the maximal OD₆₀₀ achieved by the *E. coli* culture expressing MBP.

e, f, CFU measurements of *E. coli* cultures expressing GVs under the dual-inducer system. Cultures were induced with strategy in **a** (**e**) or in **b** (**f**). As controls, CFU measurements were performed on cultures expressing wild-type pNL29 GVs or MBP under 20 µM IPTG induction. Representative plates are shown in **Supplementary Fig. 8a** and **9a**.

g, Heatmap of cell viability of *E. coli* cultures expressing GVs under the dual-inducer system. The cells were harvested at predetermined time points post-induction and analyzed by flow cytometry (SYTO-9 vs. PI). Comprehensive flow cytometry plots are shown in **Supplementary Fig. 8d** and **9d**.

Absorbance values (y-axis) in **c** and **d** are reported in absorbance units (AU). Data in **c** and **d** represent mean ± s.d. for $n = 6$ biologically independent samples, and in **e** and **f** represent mean ± s.d. for $n = 3$ biologically independent samples for all groups.

ARTICLE IN PRESS

ARTICLE IN PRESS

Fig. 6 | Interchanging regulatory control of assembly factor proteins and shell protein expression resulted in limited mitigation of proteotoxic stress.

a, Schematic representation of the interchanged dual-inducer system for independent control of GV shell and assembly proteins. The shell protein gene is driven by an IPTG--inducible T7 promoter, whereas assembly protein genes are under a TetR-repressed, aTc-inducible promoter.

b, d, Schematic representation of the genetic construct for GV expression under the interchanged dual-inducer transcriptional system. Cultures were induced with varying concentrations of IPTG while maintaining aTc at a constant concentration (**b**), or with varying concentrations of aTc while maintaining IPTG at a constant concentration (**d**).

c, e, Growth profiles of *E. coli* cultures expressing GVs under the interchanged dual-inducer system after being induced with inducing strategies in **b** (**c**) and **d** (**e**). The growth profile of WT 20 μ M IPTG served as a control (WT). The vertical grey dashed line indicates the time point at which IPTG was introduced. The horizontal black dashed line is the same reference line as in **Fig. 5c, d**.

f, g, CFU measurements of *E. coli* cultures expressing GVs under the interchanged dual-inducer system. Cultures were induced with strategy in **b** (**f**) or in **d** (**g**). Controls are the same in **Fig. 5e, f**. Representative plates are shown in **Supplementary Fig. 10a** and **11a**.

h, Heatmap of cell viability of *E. coli* cultures expressing GVs under the interchanged dual-inducer system. The cells were harvested at predetermined time points post-induction and analyzed by flow cytometry (SYTO-9 vs. PI). Comprehensive flow cytometry plots are shown in **Supplementary Fig. 10d** and **11d**.

Absorbance values (y-axis) in **c** and **e** are reported in absorbance units (AU). Data in **c** and **e** represent mean \pm s.d. for $n = 6$ biologically independent samples, and in **f** and **g** represent mean \pm s.d. for $n = 3$ biologically independent samples for all groups.

Fig. 7 | Quantitative assessment of GV yield in *E. coli* by hydrostatic collapse assay.

a, Schematic representation of the hydrostatic collapse assay setup used to analyze GV samples. The system comprises a Nitrogen (N_2) tank with a pressure controller connected to a sealed optical cuvette containing the suspended GV samples. Hydrostatic pressure is incrementally applied, and the optical density at 500 nm (OD_{500}) is monitored using a spectrophotometer to assess the collapse behavior of GVs under increasing pressure.

b, Schematic representation and representative images of 6 M urea-treated wild-type pNL29 GV samples before (-) and after (+) hydrostatic collapse. The GV samples exhibit decreased turbidity, corresponding to a reduced OD_{500} value after hydrostatic collapse.

c, Hydrostatic collapse profile for purified 6 M urea-treated wild-type pNL29 GV samples. The hydrostatic collapse data were fitted using a Boltzmann sigmoidal regression model, depicted as a grey curve, yielding a coefficient of determination (R^2) of 0.9437.

d, e, f, Hydrostatic collapse profiles of wild-type pNL29 GV-operon-expressing *E. coli* cultures. Cultures were induced with 0 μ M (d), 200 μ M (e), and 400 μ M (f) IPTG. WT 20 μ M IPTG serves as the control. Data represent mean \pm s.d for $n = 6$ biologically independent samples. All data were fitted using a Boltzmann sigmoidal regression model (curves with respective colors), with corresponding R^2 values indicated for each IPTG concentration.

Normalized absorbance values in **c**, **d**, **e**, and **f** are expressed in absorbance units (AU) on the *y-axis*. Data in **c**, **d**, **e**, and **f** represent mean \pm s.d for $n = 6$ biologically independent samples for all groups.

ARTICLE IN PRESS

ARTICLE IN PRESS

Fig. 8 | The dual-inducer system achieves GV yields comparable to the wild-type operon.

a, c, Hydrostatic collapse profiles of *E. coli* cultures expressing GVs under the dual-inducer system. Cultures were induced using the strategies shown in **Fig. 5a (a)** and **5b (c)**. WT 20 μ M IPTG served as the control.

b, d, Normalized reduction in OD₅₀₀ values of *E. coli* cultures expressing GVs under the dual-inducer system with conditions in **Fig. 5a (b)** and **5b (d)**. Statistical analysis was performed against WT 20 μ M IPTG using Brown–Forsythe and Welch one-way ANOVA tests, followed by Dunnett T3 multiple comparisons correction. **(b)** $P = 0.0028$ for 0 μ M IPTG (with 500 ng/mL aTc) and NS for all the other groups against WT 20 μ M IPTG. **(d)** $P = 0.0004$ and $P = 0.0040$ for 0 and 50 ng/mL aTc (with 200 μ M IPTG) and NS for all the other groups against WT 20 μ M IPTG.

e, Schematic representation of the buoyancy-based purification procedure for GV samples.

f, Normalized OD₅₀₀ values of purified GVs from groups exhibiting high GV yield in **b** and **d**. Statistical analysis was performed against WT 20 μ M IPTG using Brown–Forsythe and Welch one-way ANOVA tests, followed by Dunnett T3 multiple comparisons correction. $P = 0.0108$ for 1000 ng/mL aTc (with 200 μ M IPTG) and NS for all the other groups against WT 20 μ M IPTG.

g, h Hydrostatic collapse profiles of *E. coli* cultures expressing GVs under the interchanged system (**Fig. 6a**). **(g)** Cultures were induced using the strategies shown in **Fig. 6b (g)** and **6d (h)**. WT 20 μ M IPTG serves as the control.

Normalized absorbance values (y-axis) in **a, c, g**, and **h** are expressed in absorbance units (AU). Data in **a, b, c, d, f, g**, and **h** represent mean \pm s.d for $n = 6$ biologically independent samples for all groups. All data in **a, c, g**, and **h** were fitted using a Boltzmann sigmoidal regression model (curves with respective colors), with corresponding R^2 values indicated for each IPTG **(a)** **(g)** or aTc **(c)** **(h)** concentration.

Fig. 9 | Screening induction timing between assembly factors and shell protein expression reveals an optimal window for maximizing bacterial growth and GV yield.

a, Schematic timeline of dual-inducer schedules for assembly factor and shell protein expression (see Methods).

b, Growth profiles of *E. coli* expressing GVs with aTc (-2 h) and aTc (-1 h). Grey dashed lines mark IPTG induction; colored solid lines mark aTc addition. Data are mean \pm s.d. ($n = 5$). Individual curves are in **Supplementary Fig. 11**.

c, CFU measurements of *E. coli* in **b**. Controls are the same in **Fig. 5e, f**. Data are mean \pm s.d.; $n = 5$ for temporal-induction groups and $n = 3$ for controls.

d, Heatmap of cell viability of *E. coli* in **b**.

e, Normalized OD₅₀₀ of purified GVs (mean \pm s.d.; -2 h and -1 h groups, $n = 3$; WT, $n = 6$).

f, Growth profiles of *E. coli* using various temporal induction strategies (mean \pm s.d. for $n = 5$ for all; WT, $n = 6$). In “IPTG (start)”, the blue line marks IPTG present from inoculation; the grey line marks aTc addition. The horizontal black dashed line matches that in **Fig. 5c, d**.

g, CFU measurements of *E. coli* in **f**. Controls are the same in **c**. Data represent mean \pm s.d. from $n = 3$ for all groups.

h, Heatmap of cell viability of *E. coli* in **f**.

i, Normalized OD₅₀₀ of purified GVs (mean \pm s.d.; $n = 5$ for all; WT, $n = 6$).

Absorbance in **b, f**, and normalized absorbance in **e, i** are plotted in absorbance units (AU, y-axis). Data in **b, c, e, f, g**, and **i** are from biologically independent samples (n indicated). Statistics in **e** and **i** are vs WT using Brown–Forsythe and Welch one-way ANOVA with Dunnett T3: $P = 0.0017$ and 0.0010 for aTc (-2 h) and (-1 h) (**e**); $P = 0.0034$, 0.0032 , 0.0051 for 4, 5, and 6 h intervals, all other groups NS (**i**). Comprehensive flow cytometry plots for **d** and **h** are in **Supplementary Fig. 14b**.

Editorial Summary

Gas vesicle protein nanostructures can damage host bacteria when strongly expressed. Here, authors

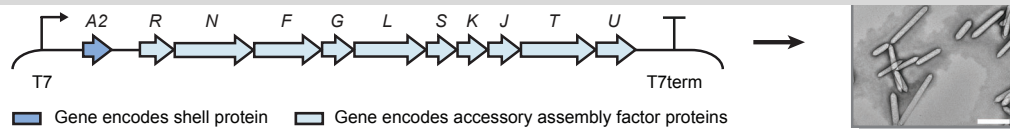
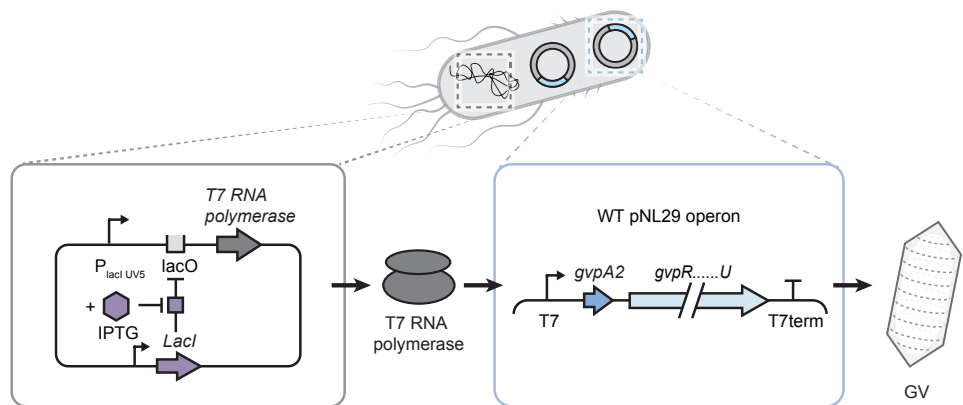
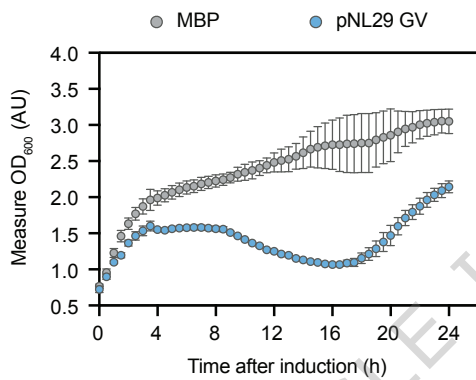
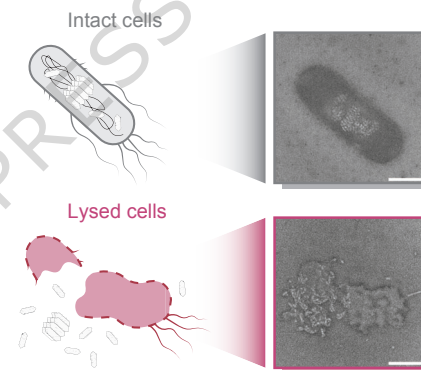
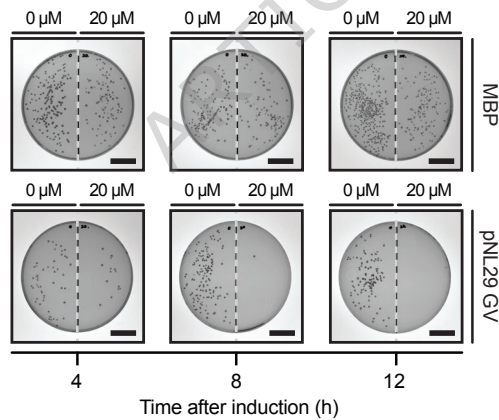
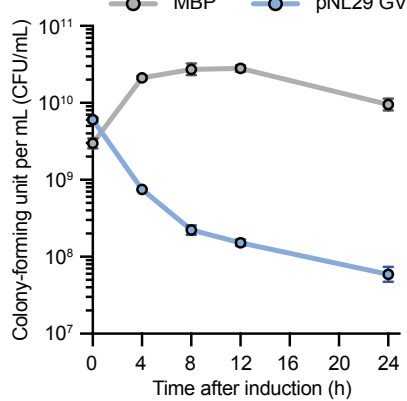
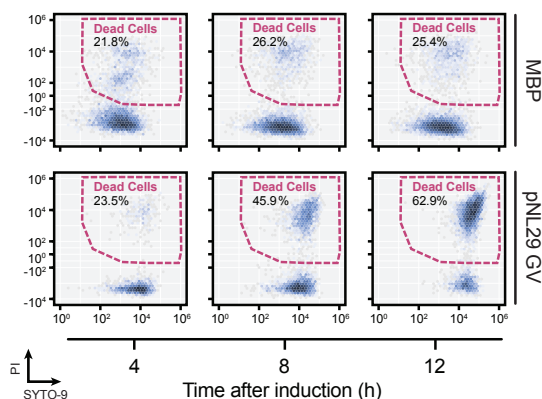
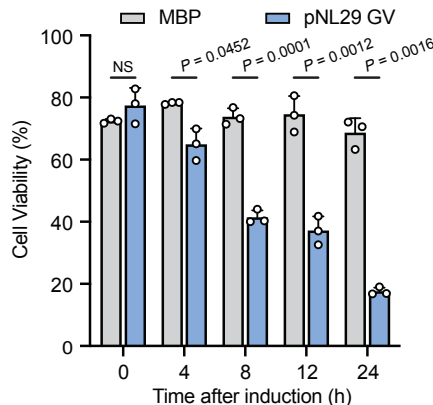
develop a dual-inducer timing circuit that pre-expresses assembly-factor proteins, limiting toxic aggregation while maintaining gas vesicle production.

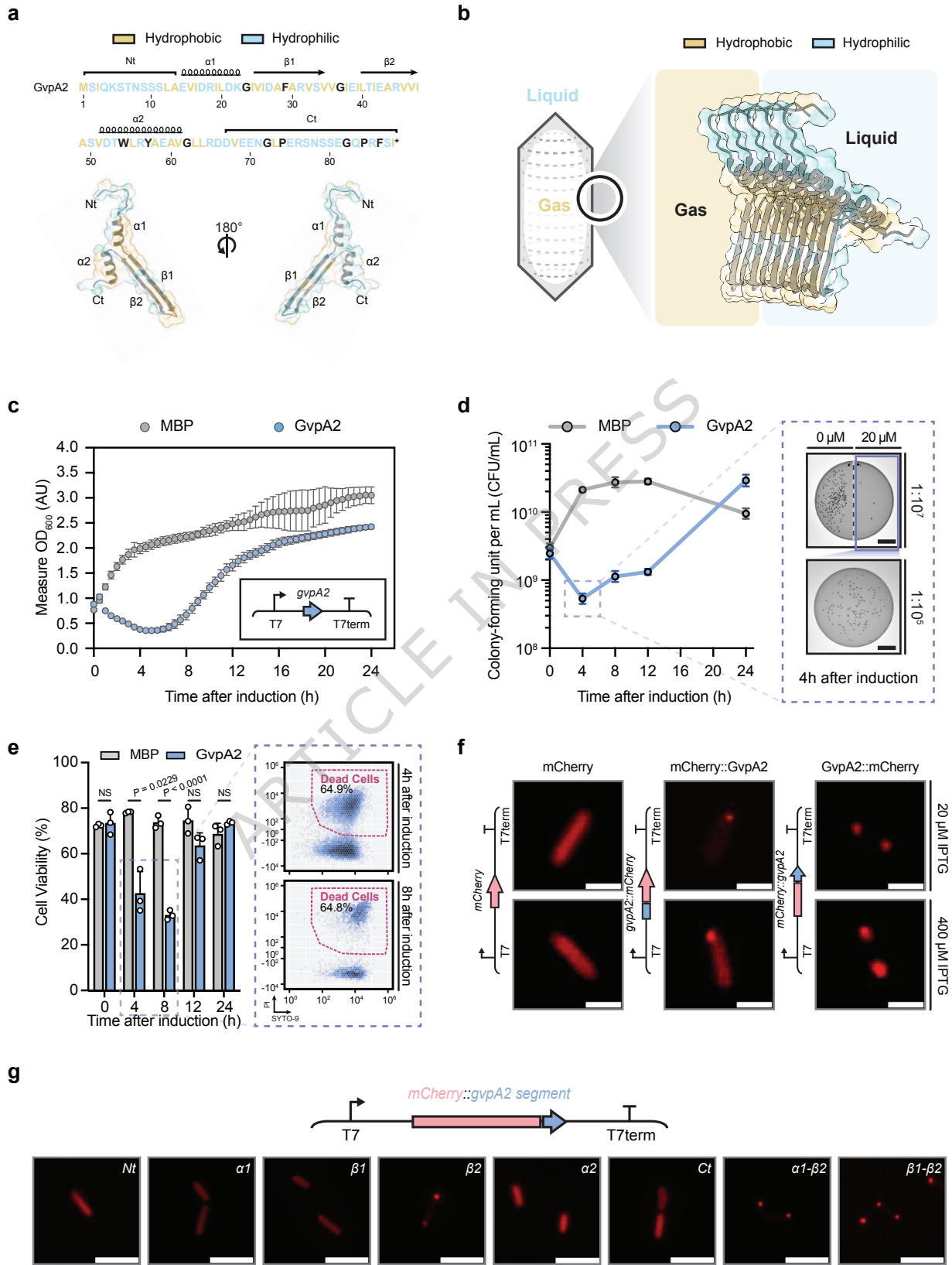
Peer Review Information: *Nature Communications* thanks Fei Yan, and the other, anonymous, reviewer(s) for their contribution to the peer review of this work. A peer review file is available.

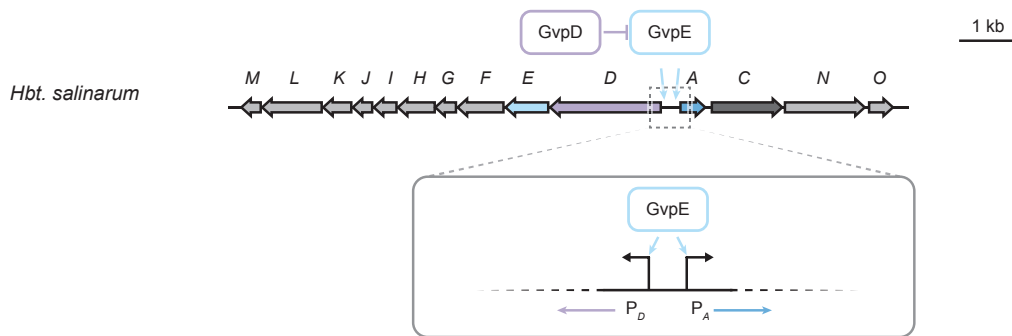
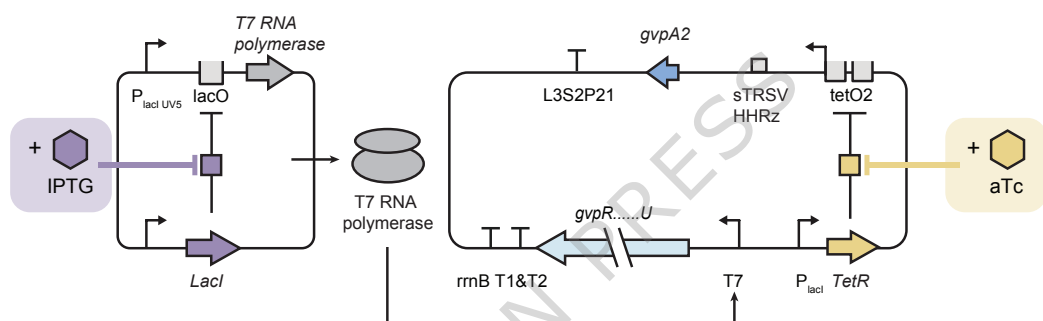
ARTICLE IN PRESS

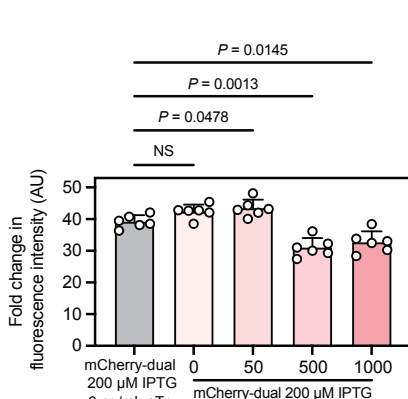
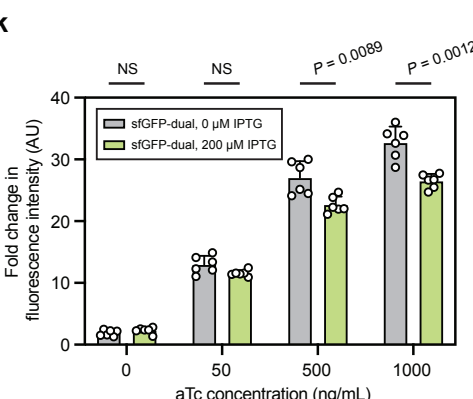
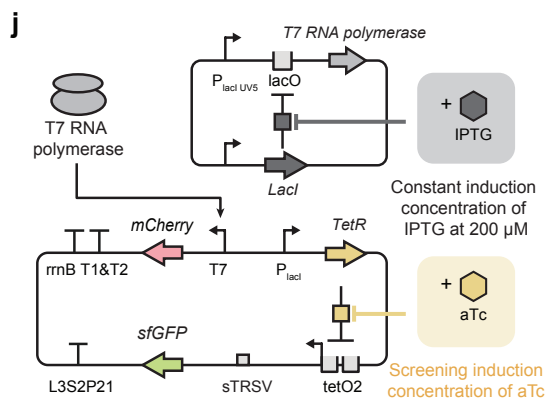
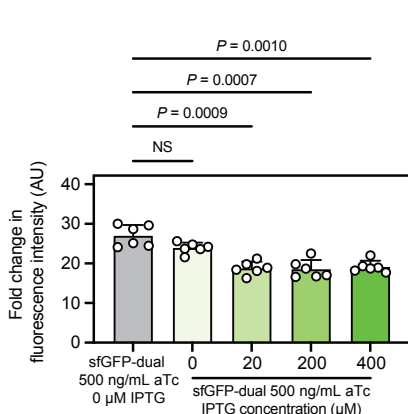
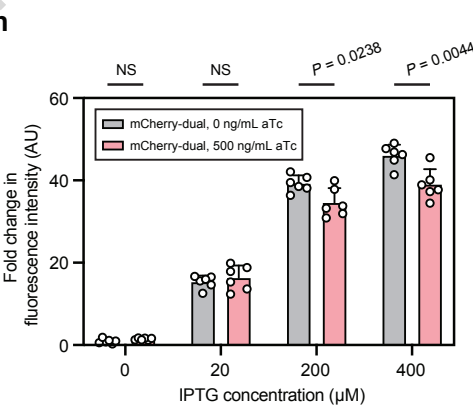
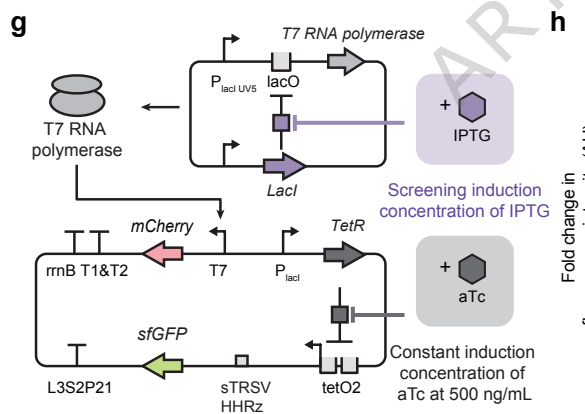
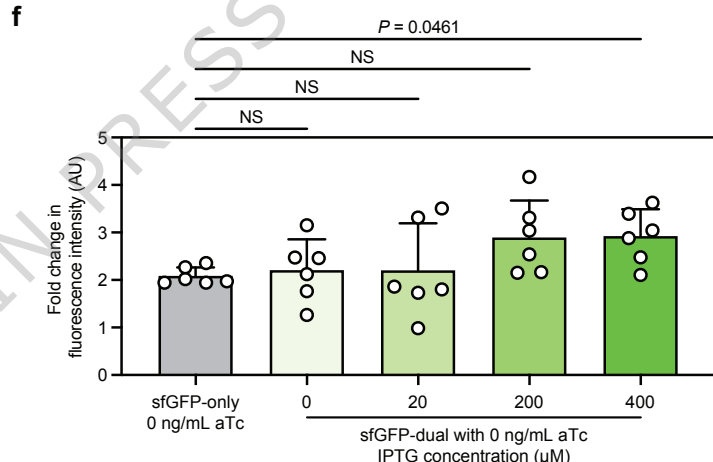
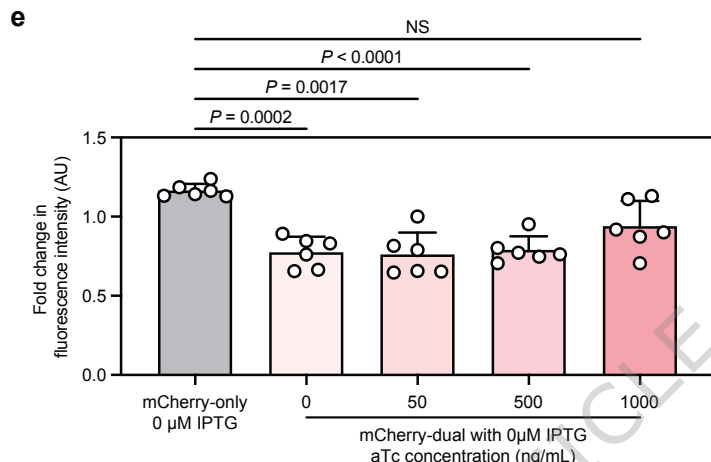
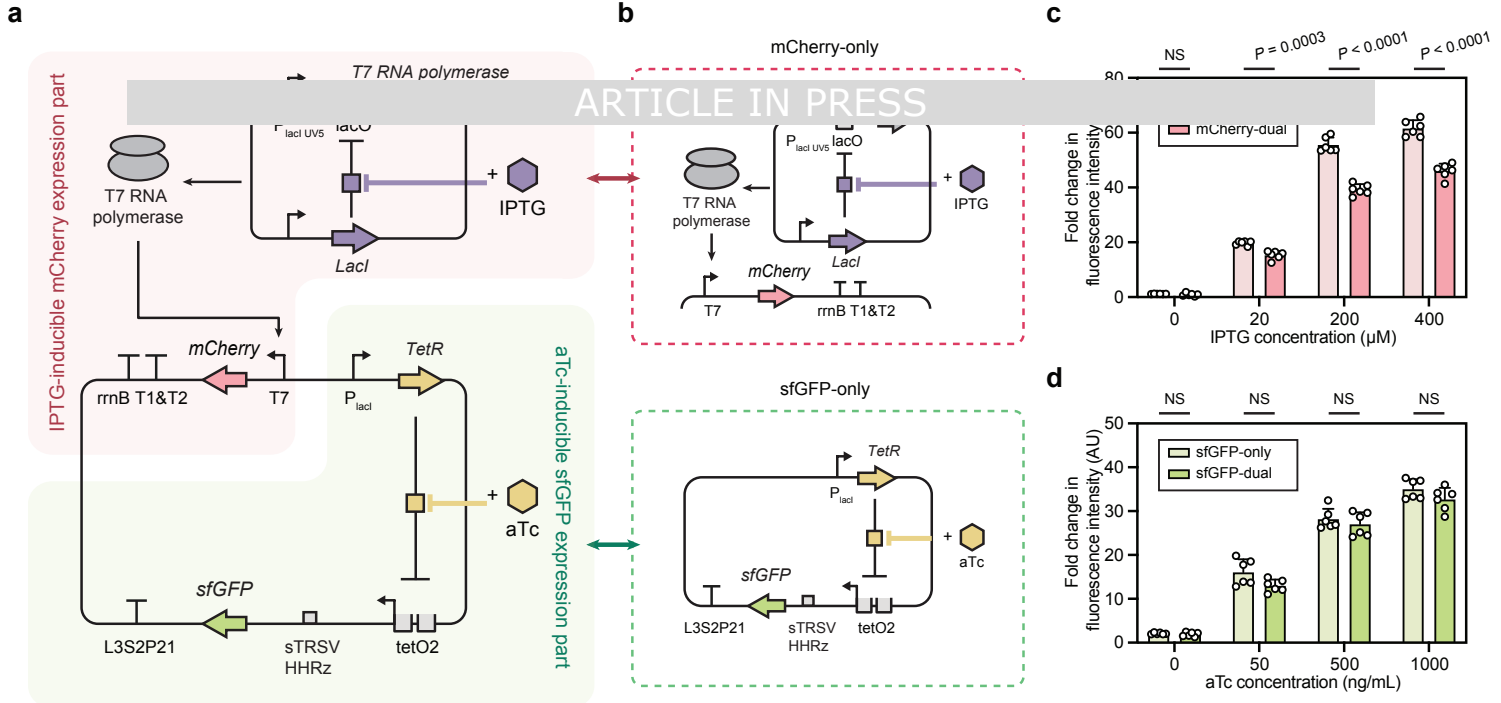
a

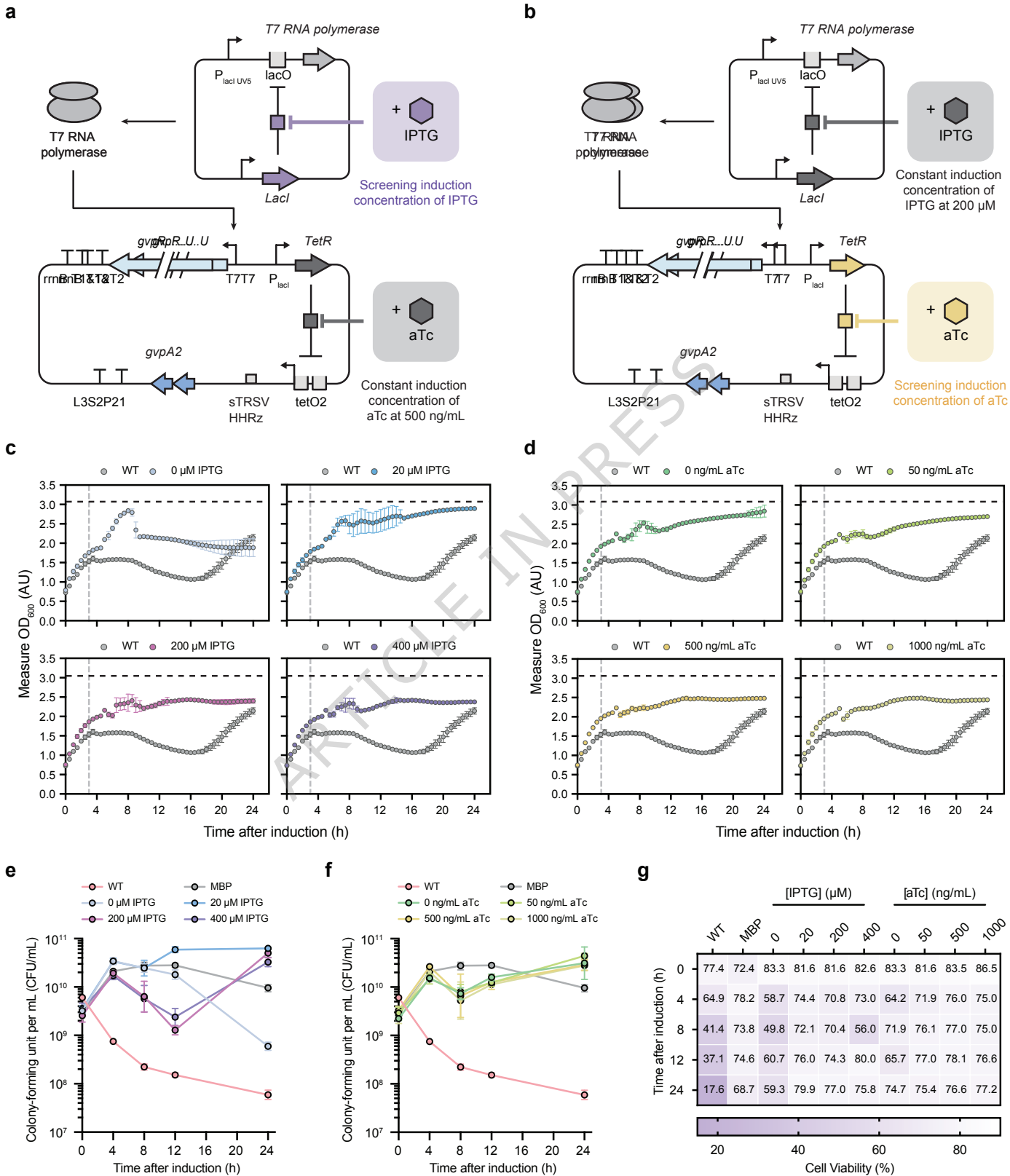
ARTICLE IN PRESS

**b****c****d****e****f****g****h****i**



a**b**





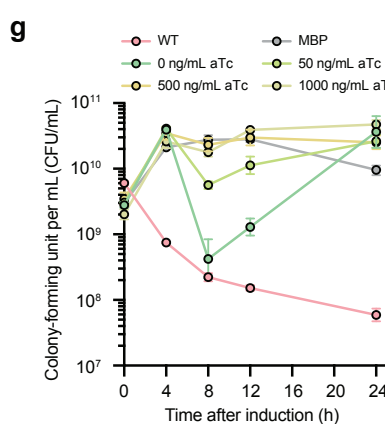
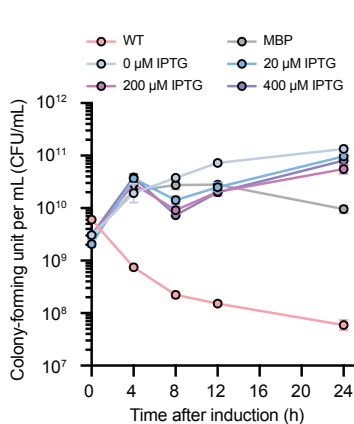
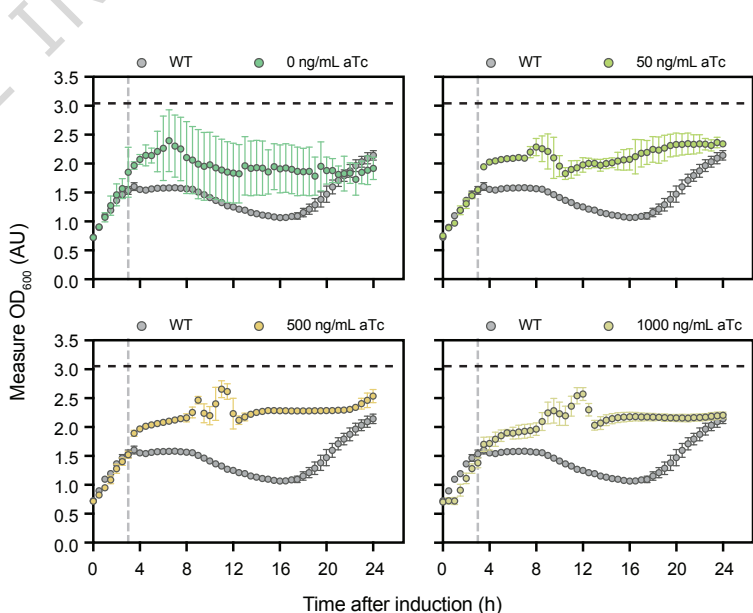
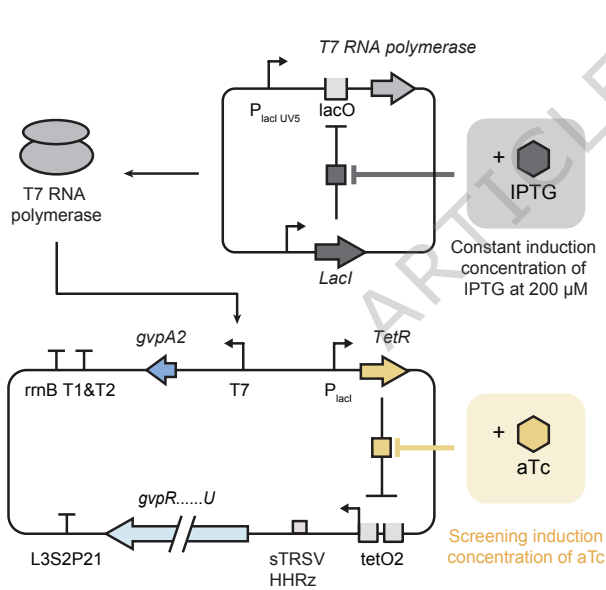
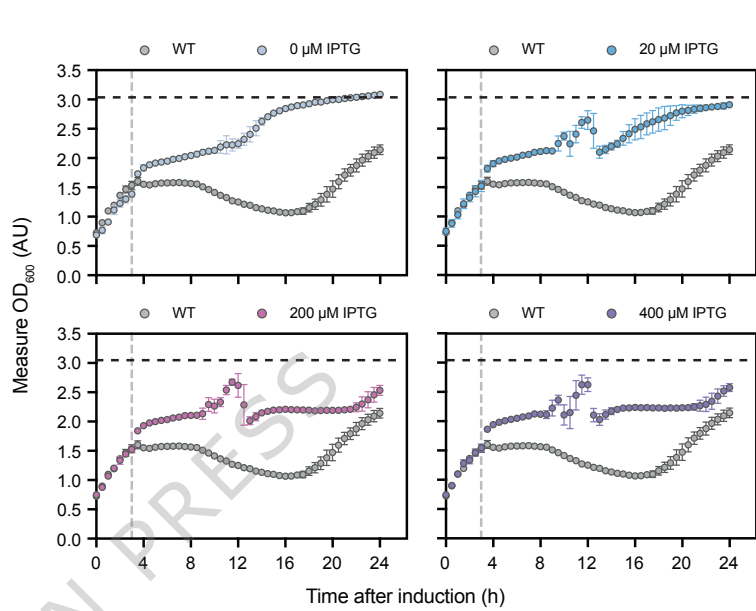
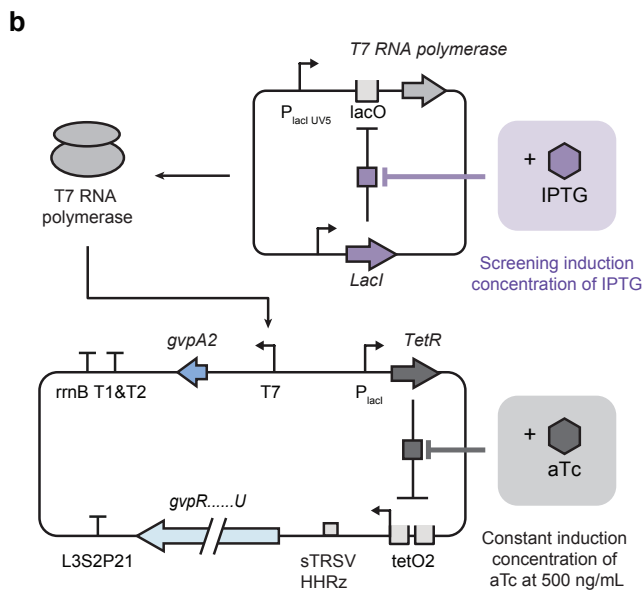
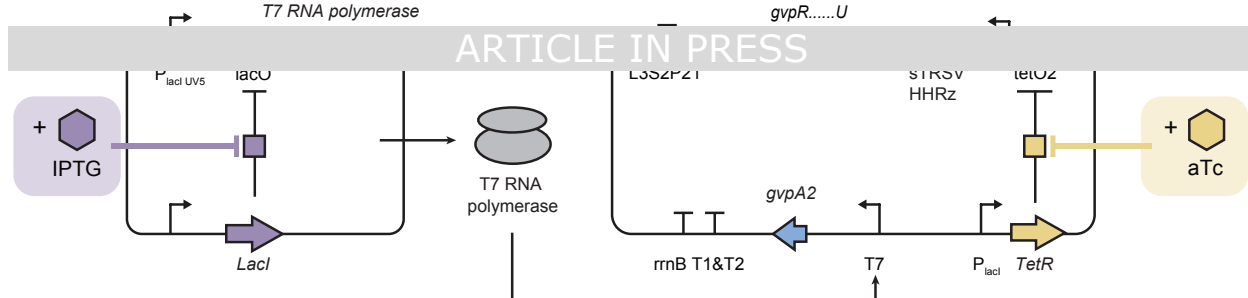
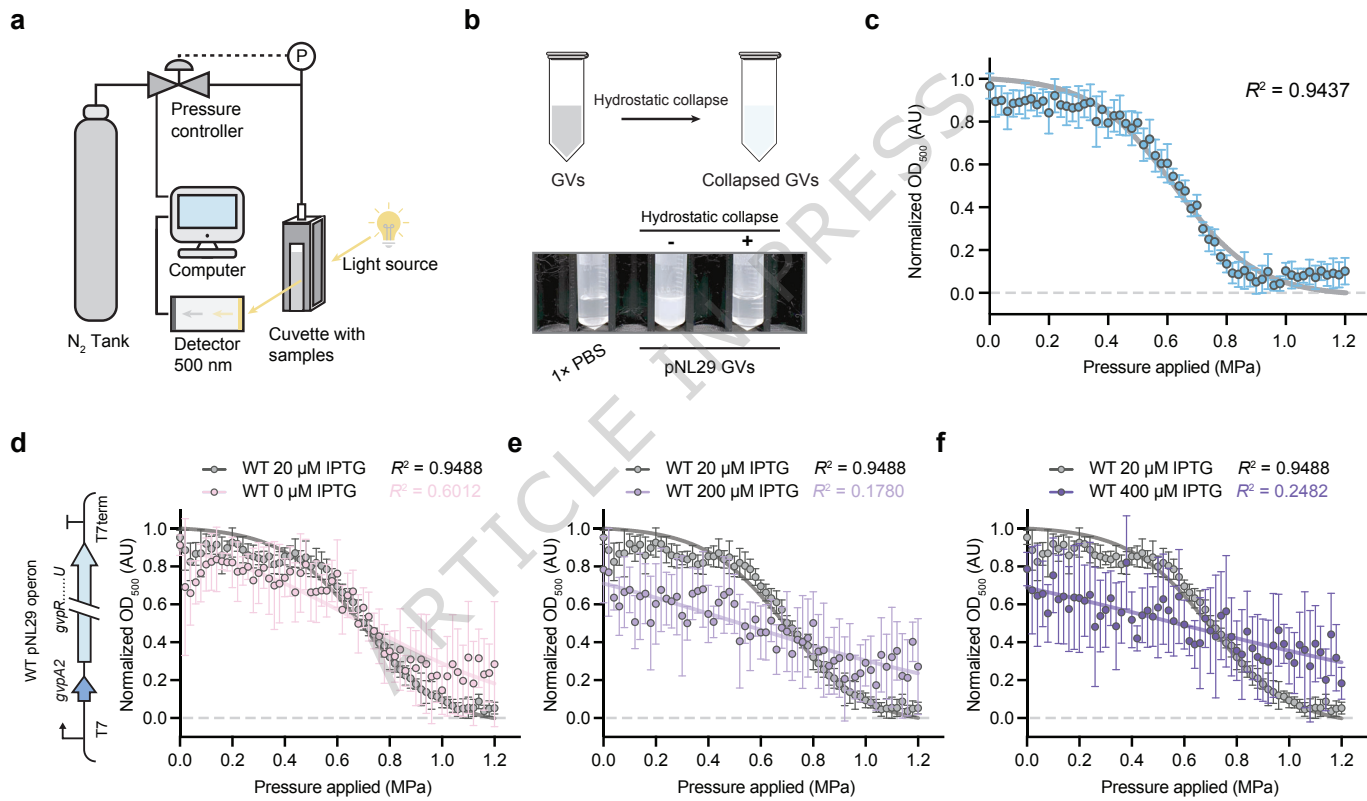
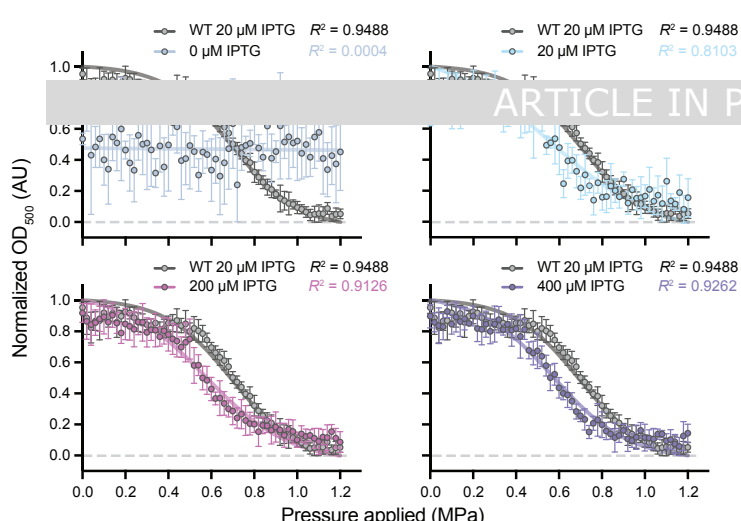
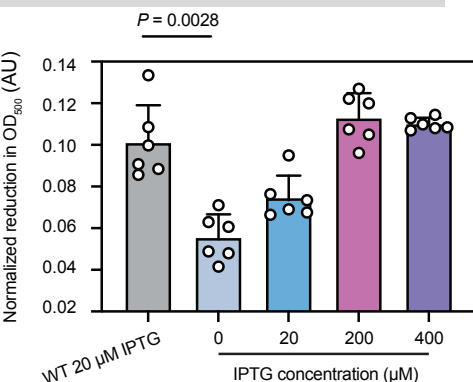
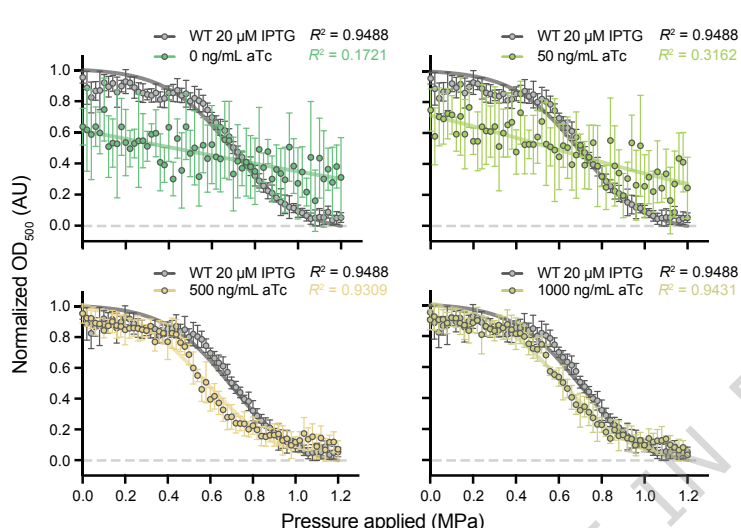
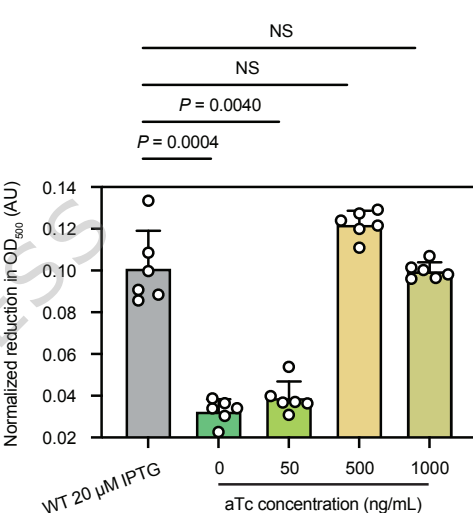
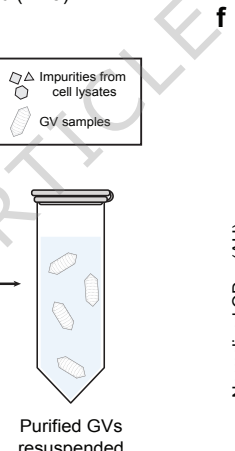
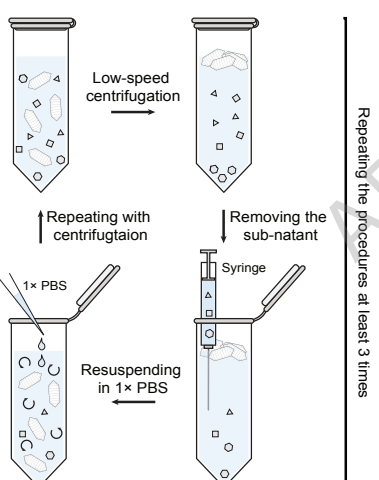
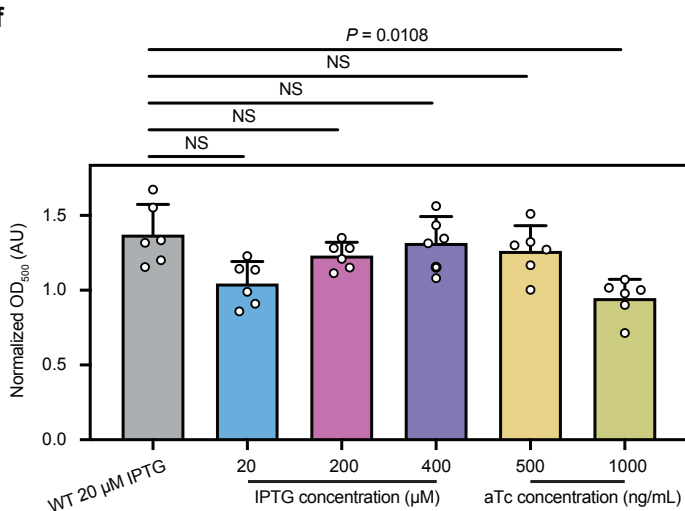
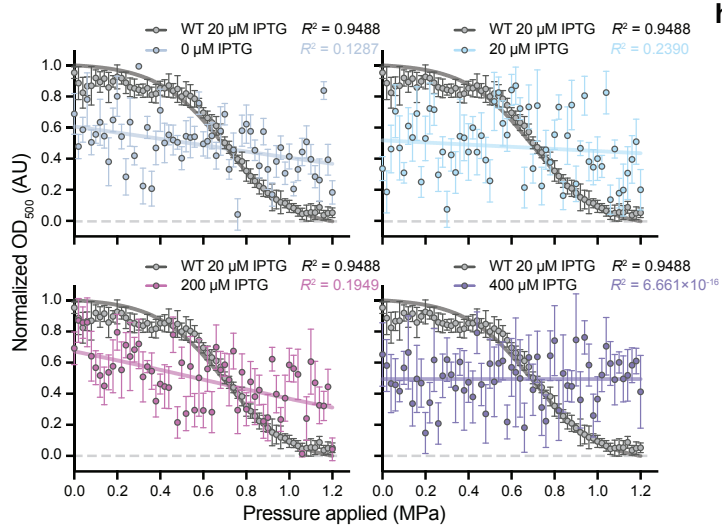


Figure 2 is a heatmap showing cell viability (%) as a function of time after induction (h) and concentration of inducer (IPTG and aTc). The x-axis represents Cell Viability (%) from 20 to 80. The y-axis represents Time after induction (h) with values 0, 4, 8, 12, and 24. The z-axis shows two sets of conditions: [IPTG] (0, 20, 200, 400) and [aTc] (0, 50, 500, 1000). The color scale ranges from light yellow (high viability) to dark purple (low viability). A legend at the bottom indicates that darker shades of purple represent lower cell viability.

Time after induction (h)	[IPTG] (μM)				[aTc] (ng/mL)					
	0	20	200	400	0	50	500	1000		
0	77.4	72.4	89.2	87.5	87.3	88.3	88.3	91.3	87.9	87.4
4	64.9	78.2	71.4	71.2	64.1	63.0	66.3	62.1	57.3	63.1
8	41.4	73.8	69.2	61.3	44.4	50.7	62.4	67.4	52.3	52.3
12	37.1	74.6	70.0	67.2	72.6	71.3	67.8	70.7	69.4	65.2
24	17.6	68.7	67.8	76.0	74.0	74.6	60.4	69.5	68.8	75.0



a**b****c****d****e****f****g****h**